PHYSICAL REVIEW SPECIAL TOPICS - ACCELERATORS AND BEAMS **13**, 022002 (2010)

High field Q slope and the baking effect: Review of recent experimental results and new data on Nb heat treatments

G. Ciovati,[1,*] G. Myneni,[1] F. Stevie,[2] P. Maheshwari,[2] and D. Griffis[2]
[1]*Thomas Jefferson National Accelerator Facility, Newport News, Virginia 23606, USA*
[2]*North Carolina State University, Raleigh, North Carolina 27695, USA*
(Received 25 November 2009; published 22 February 2010)

The performance of superconducting radio-frequency (SRF) cavities made of bulk Nb at high fields (peak surface magnetic field greater than about 90 mT) is characterized by exponentially increasing rf losses (high-field Q slope), in the absence of field emission, which are often mitigated by low-temperature (100–140°C, 12–48 h) baking. In this contribution, recent experimental results and phenomenological models to explain this effect will be briefly reviewed. New experimental results on the high-field Q slope will be presented for cavities that had been heat treated in a vacuum furnace at high temperature without subsequent chemical etching. These studies are aimed at understanding the role of hydrogen on the high-field Q slope and at the passivation of the Nb surface during heat treatment. Improvement of the cavity performances, particularly of the cavities' quality factor, have been obtained following the high-temperature heat treatments, while secondary ion mass spectroscopy surface analysis measurements on Nb samples treated with the cavities revealed significantly lower hydrogen concentration than for samples that followed standard cavity treatments.

DOI: 10.1103/PhysRevSTAB.13.022002 PACS numbers: 74.25.N−, 74.70.Ad, 74.25.Uv, 85.25.−j

I. INTRODUCTION

The use of superconducting rf (gigahertz range) cavities made of high-purity (residual resistivity ratio >200) bulk niobium has been increasing steadily over the past decade, as these cavities are being employed in a growing number of accelerator facilities all over the world for applications that range from basic energy science to high-energy physics. This demand requires continuous improvement of the cavity performance, both in terms of higher quality factors (to reduce cryogenic losses) and higher accelerating gradients (to reduce the real-estate gradient of high-energy accelerators).

The most outstanding issue related to the basic understanding of the superconductivity of high-purity, bulk Nb in strong rf fields is the occurrence of a sharp increase of the rf losses when the peak magnetic field, B_p, reaches about 90 mT, consequently limiting the operational accelerating gradient of superconducting radio-frequency (SRF) Nb cavities for particle accelerators to about 25 MV/m. This phenomenon was discovered in 1997 [1,2] after the development of improved surface cleaning techniques allowed the preparation of cavities which achieved high surface fields, without being limited by "extrinsic" losses, such as those caused by field emission.

Experiments showed that the onset of the newly discovered "anomalous" losses, which are commonly referred to as "high-field Q slope" or "Q drop," range between 80–110 mT (it has been established that the Q drop is a magnetic field phenomenon), depending on the particular material-processing combination. Lower onset of the Q drop is typically associated with "rougher" surfaces.

Currently, two types of high-purity (residual resistivity ratio greater than 200) Nb material are used for cavity fabrication: fine-grain (ASTM 5) and large (cm^2 size) grain or even single crystal. The two techniques currently used for the final surface polishing of Nb cavities are buffered chemical polishing (BCP) and electropolishing (EP).

An empirical "cure" for the Q drop had already been discovered in 1998 and consisted of a low-temperature (100–140°C, 48 h) baking of the cavities in ultrahigh vacuum [3,4]. Later experiments showed that the benefit of baking and the baking parameters (time and temperature) depend significantly on the cavity material-processing combination. These findings are summarized in [5].

A model which describes all the experimental results related to the Q drop and the baking effect has yet to be found. The solution to this problem will help devise new, possibly cheaper, ways of improving the overall performance of Nb cavities. In addition, it will give important clues to the understanding of loss mechanisms in high-temperature superconductors, comparatively more difficult to understand than Nb, which are being investigated for future SRF applications.

Several models to explain the Q drop and the baking effect had been proposed over the past decade, but strong contradictions between each one of them and experimental results were found, as more experiments to test their assumptions had been carried out over the past years. Reviews of such models and experimental results can be found in Refs. [5,6].

---

[*] gciovati@jlab.org

Temperature mapping of the cavity surface during high-power rf tests at 2 K consistently show strong, nonuniform heating occurring in the high-magnetic field area of the cavity (“equator” area), causing the Q drop [5,6]. The regions of the cavity where the strong heating occurs are referred to as “hot spots.” In one occasion, hot spots corresponding to a Q drop occurring at much lower field ($B_p \sim 30$ mT) were measured closer to the iris of a single-cell cavity made by spinning, an alternative cavity fabrication technique [7]. The hot spots moved closer to the equator as the Q drop onset increased with additional BCP. In this particular case, roughness may play a major role, as cavities made by spinning showed very rough surfaces, with macroscopic cracks visible near the iris region as a consequence of the large material deformation.

In this contribution we will briefly review theoretical and experimental results on the high-field Q slope published in the past two years. Earlier models and experimental results have been already discussed in previous reviews [5,6]. In particular, we will review two models which give a good description of the observed $Q_0(B_p)$ dependency, and a phenomenological model (so-called “oxygen pollution model”) along with results which contradict some of its hypotheses. We will then review recent theoretical and experimental results indicating a connection between the Q drop and magnetic vortices pinned or entering the Nb surface. Results on niobium samples related to the Q drop will also be discussed. All these are the subject of Sec. II of this article. Section III is a discussion on the possible role of hydrogen as a cause for the Q drop, while Sec. IV shows new cavity test results after low-temperature baking in hydrogen atmosphere. Section V presents new cavity test results and sample analysis by secondary ion mass spectrometry (SIMS) after high-temperature heat treatment followed by an attempt to passivate the Nb surface by growing a thin layer of niobium nitride by thermal diffusion. A discussion of the new experimental results is given in Sec. VI, while conclusions are given in Sec. VII.

II. REVIEW OF RECENT MODELS AND EXPERIMENTAL RESULTS RELATED TO THE HIGH-FIELD *Q* SLOPE

A. Models that describe the $Q_0(B_p)$ curves

One model which provides a good description of the $Q_0(B_p)$ curves was proposed by Gurevich [8] and it is based on an analytical solution of the 2D thermal diffusion equation which includes the extra power localized in a small defect region. Losses are caused by Joule heating of regions with higher surface resistance than the surrounding Nb. The results show that a hot spot of radius much larger than the defect size is produced. The sum of N nonoverlapping hot spots yields an expression for the global surface resistance of the cavity, which is then used in the heat balance equation for the temperature of the cavity surface exposed to rf field. The solution of such equation is expressed in the following parametric dependence $Q_0(B_p)$:

$$u(\theta) = \theta e^{1-\theta}$$

$$\frac{2B_p^2}{B_{b0}^2} = 1 + g + u(\theta) - \sqrt{[1 + g + u(\theta)]^2 - 4u(\theta)},$$

$$Q_0(B_p) = \frac{Q_0(0)e^{-\theta}}{1 + g/[1 - (B_p/B_{b0})^2]}, \tag{1}$$

where g, $Q_0(0)$, and B_{b0} are fit parameters. g is a parameter which is related to the number and intensity of hot spots, $Q_0(0)$ is the Q_0 value at low field, and B_{b0} is the thermal breakdown field in absence of defects.

A recent model proposed by Weingarten [9] gives an expression for a field-dependent surface resistance obtained assuming that defects of density n_{s0} with smaller values of the lower critical field (B_0) than Nb are present on the surface and that the size of the normal conducting regions increases with increasing magnetic field, above B_0. Increase of the surface resistance is due to the increase of the condensation energy density due to the loss of Cooper pairs by loss of volume. The field-dependent surface resistance given in [9] is an infinite product expansion:

$$R_s^{nl}(B_p) = \frac{4}{3}\pi\mu_0\lambda^3 f n_{s0}\left\{\left(\frac{B_0}{B_p}\right)^2 + \frac{1}{2}\left(\frac{B_p}{B_c}\right)^2 \times \left[1 + \frac{2}{3}\kappa^2\left(\frac{B_p}{B_c}\right)^2\left(1 + \frac{3}{4}\kappa^2\left(\frac{B_p}{B_c}\right)^2 \times \cdots\right)\right]\right\}, \tag{2}$$

where the first term in the sum describes the low-field Q increase while the second term describes the medium and high-field Q slopes. λ is the penetration depth, B_c is the

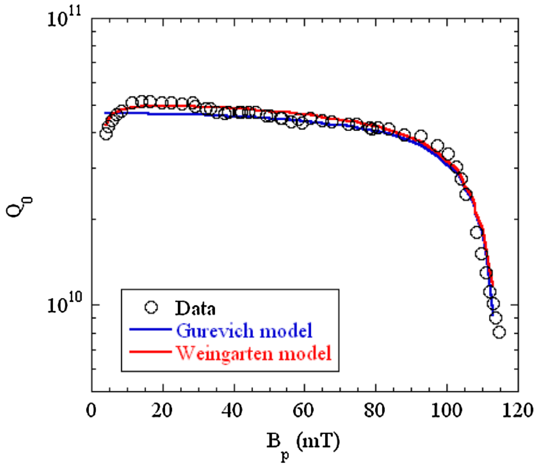

FIG. 1. (Color) Typical $Q_0(B_p)$ curve of a bulk Nb cavity limited by the Q drop fitted with Gurevich and Weingarten models. The data are from a CEBAF single-cell cavity (1.47 GHz) measured at 1.4 K [10].

TABLE I. Fit parameters and fit correlation factor for Gurevich and Weingarten models applied to the data shown in Fig. 1. Values of $\lambda = 36$ nm and $B_c = 190$ mT were used in Eq. (2).

Gurevich model		Weingarten model	
$Q_0(0)$	5.5×10^{10}	$R_{\rm res}$ (nΩ)	5
B_{b0} (mT)	115	B_0 (mT)	1.5
g	0.18	n_{s0} $(1/m^2)$	2×10^{10}
r^2	0.960	κ	1.767
		r^2	0.985

thermodynamic critical field at the He bath temperature, f is the resonant frequency, and κ is the Ginzburg-Landau parameter. The expression in Eq. (2) is added to the BCS and residual resistance to determine the total surface resistance, $R_s(B_p)$. The cavity quality factor is then calculated through the usual relation $Q_0 = G/R_s$. κ, n_{s0}, B_0 and the residual resistance, $R_{\rm res}$, are used as fit parameters.

Figure 1 shows, as an example, the $Q_0(B_p)$ data at 1.4 K for a typical bulk Nb cavity affected by the Q drop and the curve fits using the two models mentioned above. The data are taken from [10]. The fit parameters of the two models and the fit correlation factor, r^2, are reported in Table I. Both models provide a good description of the data with reasonable values of the fit parameters. It should be mentioned that 25 terms of the product expansion in Eq. (2) were needed for a good fit using the Weingarten model [11].

Although both models mentioned in this section give a good description of the $Q_0(B_p)$ curves, the question of what are the "defects" which cause the hot spots remains unanswered.

B. "Oxygen pollution" model

A recent model which attempts to explain the physical origins of the hot spots causing the Q drop is the so-called "oxygen pollution" model. The idea that a pollution layer at the Nb surface is involved in the Q drop and the baking effect had been already put forward by Safa in 2001 [12]. Oxygen is the impurity whose diffusion length in Nb is comparable to the rf penetration depth, for the typical baking parameters. Oxygen concentrations high enough to change the superconducting properties of Nb had been measured at the Nb/oxide interface by surface analytical methods. A refinement of the model includes the effects of both oxygen diffusion and oxide decomposition in determining the oxygen concentration at the metal/oxide interface, after the low-temperature baking [13]. The calculation shows a minimum of the oxygen concentration in the temperature range 120°–150°C for a 48 h long bakeout, in good agreement with the baking parameters which give the highest improvement of the cavity performance. The diffusion mechanism is also consistent with the following experimental results: (i) The onset of the Q drop increases continuously by increasing the baking time from 3 to 60 h [14]. (ii) The BCS surface resistance decreases continuously by increasing the baking time from 3 to 48 h [3].

According to the oxygen pollution model, the hot spots are caused by magnetic vortices being pushed in the Nb surface at a B_p value corresponding to the onset of the Q drop. Regions with high concentration of interstitial oxygen (grain boundaries, for example) result in a local reduction of the surface barrier, from the value of H_{c1} of pure Nb (~ 170 mT at 2 K) down to the Q drop onset, at about 100 mT. Another mechanism which is also known to lower the surface barrier is roughness: this may explain why the Q drop onset is typically lower in BCP-treated cavities than EP-treated ones (for fine-grain Nb).

Baking at 120°C, for 12 to 48 h, depending on the grain boundary density, dilutes the interstitial oxygen near the surface over a larger volume, effectively lowering its concentration within the rf penetration depth. This effect will push the surface barrier against vortex penetration to higher values, toward H_{c1} of pure Nb.

In the past two years, experiments were carried out at various laboratories to further test the oxygen pollution model and the results are in contradiction with the model predictions. In particular, the following results have been reported: (i) The Q drop was not reestablished in a previously baked cavity, after additional baking at 120°C/48 h in 1 atm of pure oxygen. Measurements on samples by secondary ion mass spectrometry (SIMS) confirmed the presence of a higher oxygen concentration at the Nb surface after baking in oxygen atmosphere [15]. (ii) The Q drop did not improve after baking a cavity *in situ* at 400°C/2 h, although the interstitial oxygen should have diffused deeper into the bulk by baking at such high

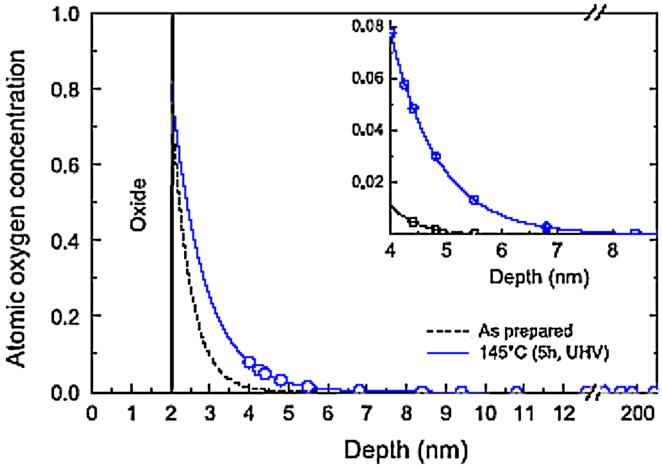

FIG. 2. (Color) Atomic oxygen concentration profile as a function of depth into Nb below the oxide layer, measured using x-ray diffuse scattering on a single-crystal Nb sample before and after baking. The figure is taken from Ref. [17].

temperature [16]. (iii) Measurements of the subsurface oxygen profile by diffuse x-ray scattering on a single-crystal Nb sample revealed a diffusion length of only about 2 nm after baking at 145°C/5 h, in spite of the 40 nm diffusion length as calculated using the diffusion equation [17]. This result, shown in Fig. 2, is explained as oxygen segregation towards the surface during cooldown to room temperature balances the diffusion at 145°C. Nevertheless, diffusion can occur at much higher rate along grain boundaries than within a single grain.

While the role of oxygen as the impurity leading to the Q drop is significantly diminished by the experimental results mentioned above, recent theoretical and experimental work [18,19] still support the idea that the hot spots are caused by magnetic vortices oscillating at the Nb surface under the action of the rf field. These findings will be discussed briefly in what follows.

C. Hot spots due to magnetic vortices

Theoretical calculations show that rf losses due to the motion of vortices at the Nb surface can certainly generate hot spots at high field, which cause the cavity quality factor to drop [18]. There are two possible ways in which vortices can cause losses at the Nb surface: (i) Vortices with segments pinned near the surface oscillate under the Lorentz force given by the rf field, causing losses. (ii) Vortices can be pushed into the surface when the amplitude of the rf field exceeds the local surface barrier. The periodic motion of such vortices produces losses.

These phenomena will be discussed more in detail in what follows.

1. Losses due to pinned vortices

Because of the incomplete Meissner effect in technical Nb, trapped vortices are always present upon cooling a Nb cavity below T_c, in the presence of a residual DC magnetic field. The resulting distribution of pinned vortices can be highly inhomogeneous and the pinning efficiency depends on the treatments applied to the Nb. Figure 3 shows a schematic representation of a vortex pinned near the surface: the pinned vortex segments oscillate under the action of the rf field. By solving the equation of motion of the pinned vortex segments, the dissipated power can then be calculated [18].

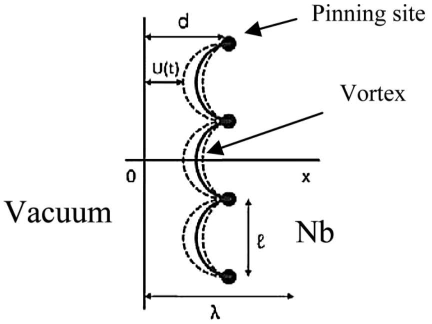

FIG. 3. Vortex pinned by a chain of defects near the surface. The solid line shows the equilibrium vortex shape due to competition of pinning and image attraction forces. The dashed lines show instantaneous vortex profiles for $B(t) = B_p$ and $B(t) = -B_p$, between which the vortex line oscillates. The figure is taken from Ref. [18].

Magnetic vortices move under the action of a thermal force, proportional to the product of the vortex entropy times the local thermal gradient [20]. Pinned vortices can therefore be depinned if a thermal force greater than the pinning force is applied. The pinning strength in pure Nb is fairly weak, compared with other technical superconductors such as NbTi and Nb3Sn, making it feasible to displace vortices by applying moderate thermal gradients. An estimate of the thermal gradient $|\nabla T|_c$ needed to depin vortices at 2 K is given by [21]

$$|\nabla T|_c \cong \frac{J_c \mu_0 T_c^2}{2B_{c1}T} = 1.5\ \mathrm{K/mm}, \tag{3}$$

where $J_c = 1\ \mathrm{kA/cm^2}$ is the critical depinning current density, $B_{c1} = 170$ mT is the lower critical field at 2 K, $T_c = 9.25$ K is the critical temperature, and $T = 2$ K is the He bath temperature.

The hypothesis of hot spots being caused by pinned vortices can therefore be tested by application of a thermal gradient of the order of the value calculated with Eq. (3) across the 3 mm thick walls of a Nb SRF cavity and then a check for changes in the thermal maps of the cavity, before and after application of the thermal gradient. Experiments of this type were done recently at JLab [19] and clearly showed changes in the intensity of the hot spots, after a thermal gradient of about 0.5 K/mm was applied by heaters glued to the outer surface of a large-grain cavity. Although a proof of principle for pinned vortices as being one of the causes for the hot spots was achieved, the applied thermal gradient was not high enough to really push vortices away from the rf surface. Most likely, what happened was a redistribution of the pinned vortices over a larger area.

In order to fully test the hypothesis of pinned vortices generating hot spots and the possibility of improvement of the cavity performance by application of a high enough thermal gradient, a series of experiments are planned at JLab where a scanning laser light, directed on the inside surface of a Nb cavity, will act as a “thermal broom” to push trapped vortices deeper into the bulk.

2. Losses due to vortex penetration

At high peak surface magnetic fields, approaching the lower critical field of Nb, vortices overcome the surface barrier, locally depressed in some areas, and enter the Nb surface. The simplest way to describe this is to solve the equation of motion of a vortex subjected to the Lorentz

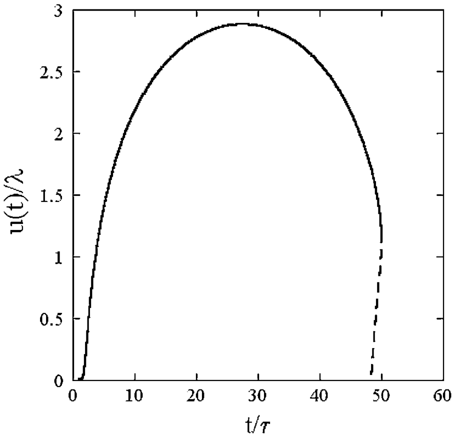

FIG. 4. Trajectory $u(t)$ of a vortex entering the surface at $B_p = B_v$ during one rf period. The dashed line shows the trajectory of an antivortex entering the surface at $-B_p = -B_v$. The figure is taken from Ref. [18].

force generated by the rf field, the image force, attracting the vortex to the surface, and the viscous drag force, opposing the motion [18]. The solution of such an equation is shown, as an example, in Fig. 4: a single vortex enters the surface when B_p exceeds the local penetration field, B_v. As the rf field changes sign, the vortex is pulled toward the surface, while an antivortex is pushed in, when $-B_p = -B_v$, and annihilates with the vortex already inside the surface. This phenomenon repeats for each rf period. It is important to notice that the calculation shows that the characteristic time, τ, it takes for the vortex to travel a distance of the order of the penetration depth is much smaller than the rf period. The maximum power, P_0, dissipated by this mechanism is twice the work done by the Lorentz force to bring a vortex from the surface deeper into the bulk:

$$P_0 = \frac{2\omega\phi_0 B_v}{\pi\mu_0}, \qquad (4)$$

$P_0 = 1.4$ W/m at 1.5 GHz and $B_v = 140$ mT.

3. *High-field losses due to vortices*

Theoretical calculations show that the local dissipation due to pinned vortices produces a long-range temperature distribution, which spreads out on the scale $\sim 2d/\pi$ (d is the cavity wall thickness). Even if these temperature variations are weak, they can nevertheless produce strong variations in the surface resistance R_s of the surrounding areas, because of the exponential dependence of R_{BCS} on temperature [18]. This nonlinear R_s can be estimated as follows:

$$R_s(r) = R_{\mathrm{BCS}}(T_0, \omega)\coth^{\sigma}\left(\frac{\pi r}{4d}\right) \qquad r > r_0 \qquad (5)$$

$$\sigma(B_p, T_0, \omega) = P_0(B_p, T_0, \omega)\frac{\Delta}{k_B \pi\kappa(T_0)T_0^2}, \qquad (6)$$

where P_0 is the dissipated power at the local heat source of size r_0, κ is the thermal conductivity, Δ is the energy gap, and T_0 is the He bath temperature.

D. Results on Nb sample measurements

While experiments and calculations highlight the contribution of magnetic vortices to high-field losses, what impurities or defects on the Nb surface are involved in this process and how the low-temperature baking affects them is still unclear. Niobium samples had been cut from the "hot" and "cold" spots of a single-cell cavity and have been analyzed at Cornell using a variety of surface analytical tools [22]. The results showed no difference in terms of surface roughness, oxide structure, or crystalline orientation between the two types of samples. What was found is that hot samples had a larger local misorientation angle than cold ones, as measured by electron backscatter diffraction (EBSD). The local misorientation angle is related to the density of lattice defects (vacancies and/or dislocations) near the surface. In addition, it was found that the local misorientation angle in hot samples is reduced by the low-temperature baking (120°C/40 h). On the other hand, preliminary results on single-crystal samples measured by positron annihilation spectroscopy (PAS) show an increase of vacancy density within the rf penetration depth after low-temperature baking [23]. These results, which are somewhat in contradiction with the Cornell results, were interpreted as due to the dissociation of vacancy-hydrogen complexes during baking.

Sample characterization by point-contact tunneling (PCT), has been done at Argonne on Nb samples prepared by EP, before and after baking [24]. The results show that unbaked samples have a high zero-bias conductance value, indicating the presence of quasiparticle states inside the superconducting energy gap, as shown in Fig. 5. The zero-bias conductance value is significantly reduced by the low-temperature baking and correlates well with the reduction of the BCS surface resistance observed on Nb cavity tests. These results are also consistent with a correlation between the amplitude of the energy gap and the Q drop onset/quench field after baking inferred from cavity test results [15]. The reduction of the zero-bias conductance value was explained by reduced scattering by magnetic impurities near the surface. Oxygen vacancies in the nonstoichiometric niobium pentoxide were proposed as the source of magnetic impurities. This interpretation somehow contradicts experimental results showing that the Q drop does not reoccur in a baked cavity after the oxide is removed with hydrofluoric acid and a new one is grown by water rinses [14]. In addition, measurements of the magnetic susceptibility in Nb samples done at DESY showed an increase of the Curie constant after baking. This was interpreted as an

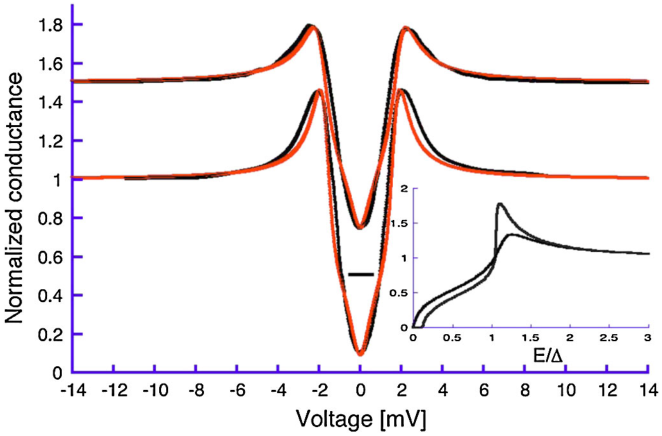

FIG. 5. (Color) In black, average conductance curves of EP (top) and vacuum baked (bottom) Nb samples, shifted for greater clarity. In red are fits with Shiba theory. Inset: Corresponding Shiba density of states. The figure is taken from Ref. [24].

increase of the concentration of localized magnetic moments near the surface [25].

III. THE POSSIBLE ROLE OF HYDROGEN

A. How hydrogen enters niobium

Niobium is an active metal that will spontaneously react with water, or water vapor, to produce hydrogen at high partial pressures. The passivating (continuous) surface niobium oxide film seals the active Nb metal from exposure to water preventing this reaction, but conditions that attack, break, or remove this film in the presence of water will result in H uptake as the water is reduced on the surface of the metal according to reactions of the form

$$x\mathrm{Nb} + y\mathrm{H_2O} \longrightarrow \mathrm{Nb}_x\mathrm{O}_y + y\mathrm{H_2}, \qquad (7)$$

where the values of the variables x and y depend on the stochiometry of the oxide produced by the reaction. These reactions can produce hydrogen at fugacities as large as 2.13×10^{25} Pa (2.1×10^{20} atm) at room temperature [26]. Therefore, processing steps such as grinding, welding, chemical, and electropolishing that remove the protective oxide in the presence of water or water vapor will result in the spontaneous reduction of water molecules to form adsorbed H atoms on the surface of Nb metal.

The equilibrium fugacity or activity of the H_2 produced by these reactions exceeds the solubility limit for H in Nb. This could result in the formation of H_2 blisters or Nb-H phases. It also exceeds that of the processing environments, and H_2 gas evolution should prevent the actual H activity on the surface from reaching these high theoretical equilibrium values. The relatively slow kinetics of recombination and H_2 bubble nucleation compared with the reduction of water molecules will still result in significant hydrogen activities and absorption. Fortunately, these reactions also produce Nb oxides that can cover the surface and seal the underlying metal from water, but these oxides will also retard or block H outgassing. The extent of H absorption will depend on the relative kinetics of these processes and the stability of the repassivating oxide in the processing environment.

The application of an anodic current, such as during the EP process, can suppress, at least theoretically, hydrogen evolution at the Nb surface [26]. However, natural perturbations to the current distribution or local shielding from the polarizing current could still result in the establishment of conditions where hydrogen evolution is favorable. This is in agreement with experimental results by the hydrogen forward scattering technique on Nb samples, showing low H contamination during EP as long as the polarizing current was applied [27].

The diffusion coefficient of hydrogen in niobium at room temperature ($\sim 5 \times 10^{-6}$ $\mathrm{cm^2/s}$) is more than 10 orders of magnitude greater than that of other impurities, such as N, C, or O; therefore hydrogen produced by the reduction of water on the Nb surface will rapidly diffuse into the bulk even at room temperature. Hydrogen occupies octahedral and tetrahedral interstitial sites of the niobium's body-centered cubic lattice. In spite of the large diffusion coefficient, there are a few factors which may lead to nonhomogeneous hydrogen distribution: (i) Higher hydrogen concentrations are found at locations of higher tensile stress, due to the hydrogen interaction with lattice defects, such as dislocations and vacancies. (ii) Impurities such as nitrogen, oxygen, and tantalum in niobium constitute hydrogen "trapping" sites.

Heat treatments will also influence the amount of hydrogen absorbed or desorbed from niobium. Heating at temperatures greater than about 250°C will cause the dissociation and reduction of the natural $\mathrm{Nb_2O_5}$ layer on the Nb surface, allowing hydrogen absorption or desorption from the metal, depending on the surrounding atmosphere. For example, hydrogen uptake in a Nb foil was achieved by baking the foil in 2×10^{-4} atm of H_2 at 250°C for 18 h [28]. Hydrogen degassing from niobium is achieved by heating at or above 600°C in UHV conditions for several hours. The equilibrium hydrogen pressure p_{H} and concentration c_{H} of hydrogen dissolved in niobium in dilute solutions as a function of temperature follow Sievert's law with the following parameters [29]:

$$\log[c(\mathrm{H})] = \frac{1}{2}\log[P(\mathrm{H_2})] - 3.81 + \frac{2000}{T}, \qquad (8)$$

where the hydrogen concentration $c(\mathrm{H})$ is in units of at. %, the pressure $P(\mathrm{H_2})$ is in units of Pa and the temperature T is in units of K. Equation (8) is valid in the range 275–2275 K and $c(\mathrm{H}) < 5$ at. %.

This type of heat treatment is commonly used to lower the bulk hydrogen concentration in niobium cavities after fabrication and heavy chemical etching. Nevertheless, a fraction of the residual hydrogen in the furnace is reabsorbed into Nb during cooldown and this is a well-known

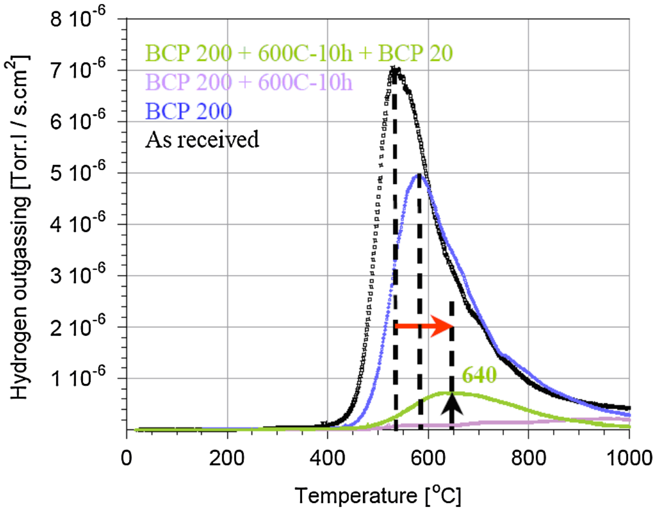

FIG. 6. (Color) Hydrogen outgassing vs temperature measured on Nb samples (RRR ~ 590) after various treatments. The black curve refers to the "as received" sample, the blue curve is after 200 μm removal by BCP, the magenta curve is after additional vacuum heat treatment at 600°C for 10 h, and the green curve is after additional 20 μm removal by BCP. The figure is taken from Ref. [31].

problem [30]. Thermal desorption spectroscopy (TDS) on high-purity Nb samples used for cavity fabrication showed [31]: (i) a hydrogen bulk desorption peak, at about 530–590°C depending on the amount of chemical etching by BCP done to the samples; (ii) the presence of a second desorption peak at higher temperature (about 700°C), possibly caused by the presence of high-energy trapping sites; (iii) the main desorption peak shifts to higher temperatures after annealing at temperatures ≥ 600°C for a duration ≥ 6 h.

Figure 6 illustrates some of the findings summarized above. The heat-treatment parameters used at DESY for hydrogen degassing are 800°C/2 h, while 600°C/10 h was developed at JLab because a reduced yield strength, due to nonuniform grain growth occurring after the heat treatment at 800°C, was measured on some batches of fine-grain Nb used for the fabrication of SRF cavities for the Spallation Neutron Source project [32].

B. Surface-included hydrogen

Higher hydrogen concentrations near the Nb surface, at the metal/oxide interface, than in the bulk were consistently measured by different techniques such as hydrogen forward scattering (HFS), glow discharge lamp (GDL), and nuclear reaction analysis (NRA). This phenomenon is due to the fact that hydrogen interacts attractively with structural imperfections (vacancies, dislocations, grain boundaries) or other interstitial impurity atoms (mainly oxygen, in this case), causing the hydrogen atom to be "trapped" at those sites. High concentration of lattice defects and interstitial oxygen is found in the near-surface region, as mention in Sec. II D. NRA measurements showed a reduction of the hydrogen concentration peak near the surface after low-temperature baking in UHV conditions, as shown in Fig. 7 [10]. The reason for this is not completely clear at this point, but it is plausible that the increased mobility of vacancy and oxygen atoms may "free" hydrogen to redistribute more uniformly throughout the bulk. It is less likely that hydrogen will be desorbed from the surface during bakeout because the natural oxide layer does not dissociate significantly up to temperature of about 200°C. TDS measurements on Nb samples baked at 145°C for 60 h showed a very small amount of released hydrogen [33].

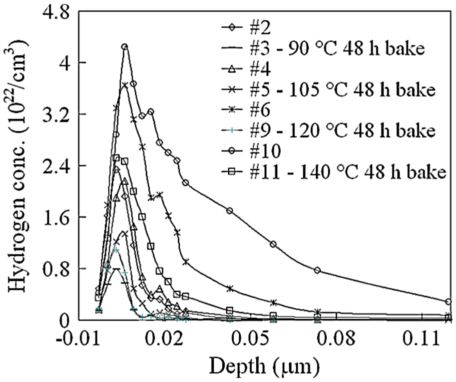

FIG. 7. Hydrogen concentration as a function of depth from the surface of Nb samples prepared by BCP, before and after low-temperature baking in UHV, as measured by NRA. The figure is taken from Ref. [10].

In what follows, we indicate several observations found in the literature which may link hydrogen to the baking effect and the sample measurement results described in Sec. II D: (i) Thermal desorption studies on Nb foils, where the natural oxide layer was removed by cycles of thermal treatments and Ar ion sputtering, showed hydrogen desorption peaks at 130°C and 198°C, interpreted as hydrogen desorption from surface and subsurface sites [34]. Several experimental [35] and theoretical studies [36] have concluded that Nb surfaces exhibit a strongly bound subsurface state of hydrogen. (ii) Measurements by positron annihilation spectroscopy (PAS) show that the defect density (vacancies) increases with hydrogen concentration in Nb samples [37]. Hydrogen entering Nb during chemical etching or mechanical polishing could actually be the source of the high defect density in the "hot spot" samples measured by EBSD. (iii) Hydrogen affects the magnetic behavior of Nb by lowering the magnetic susceptibility for increasing H concentration [38]. It is possible that hydrogen is the "magnetic impurity" invoked by the PCT results.

While these findings may suggest a link between hydrogen and the *Q* drop and the baking effect which requires deeper investigation, a more complete model of the Nb surface before and after baking would most likely involve both oxygen and hydrogen, both present in large quantities at the metal/oxide interface, and the interactions between them and with the Nb metal.

C. *Q* disease

Hydrogen received a lot of attention from the SRF community in the 1990s because of the so-called "*Q* disease" (see the review [39] and references therein). This phenomenon was characterized by the reduction of the cavities' quality factor by more than 1 order of magnitude, when the cavity was maintained in the temperature range 90–150 K for several hours during cooldown. It was found that the bulk H concentration can be increased up to about 10 wppm during the standard preparation steps of high-purity niobium cavities and that hydrogen can segregate near the surface where a lossy hydride phase (possibly υ phase at about 140 K) can nucleate. Therefore, the bulk H concentration is kept below about 5 wppm (0.046 at. %) by degassing Nb at 600–800°C for 2–10 h in a UHV furnace, as mentioned above. While all cavities are affected by *Q* drop, they do not necessarily show *Q* disease; therefore the bulk H concentration must be below 5 wppm. Nevertheless, higher concentration values have been measured near the surface, where H is tightly bound by lattice defects and impurities.

IV. CAVITY TEST RESULTS AFTER BAKING IN HYDROGEN ATMOSPHERE AND 600°C/10 h HEAT TREATMENT

The single-cell cavity used for the experiments described in this section was made of large-grain niobium from OTIC, Ningxia, China, and it has the same cell shape as the one used in the CEBAF accelerator. The resonant frequency of the TM_{010} mode is 1.47 GHz. The same cavity was used for a study reported in [15] and the baseline rf performance at 1.7 K, after postpurification at 1250°C, buffered chemical polishing (BCP), and UHV baking at 120°C, is shown in Fig. 8. The Q_0 at low field was 2.28×10^{10} and the cavity quenched at $B_p = 169$ mT, without field emission or *Q* drop. It was reported in [40] that an increase of the residual resistance was observed after exposure of a low residual resistivity ratio (RRR) niobium cavity to 1/7 atm of pure H_2 gas for 1 h. We performed a similar experiment with our high-purity large-grain Nb cavity, which was evacuated to $\sim 10^{-7}$ mbar and backfilled with scientific grade H_2 up to 1 atm, after the cavity had been stored in air for about 4 months after the baseline test. Hydrogen was left in the cavity for ~11 h at room temperature. The cavity was then high-pressure rinsed, dried in a class 10 clean room, assembled on a vertical stand with a temperature mapping system[1] and inserted in the cryostat. The rf performance at 1.7 K showed a reduction of residual resistance by about 4 nΩ and ~7% improvement in the quench field, as shown in Fig. 1. Moderate heating is visible in the equator region [Fig. 9(a)].

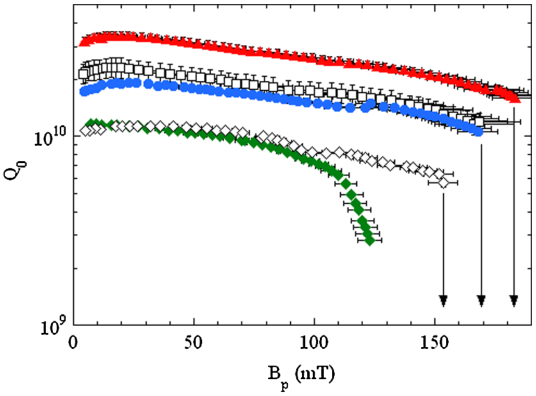

FIG. 8. (Color) Q_0 vs B_p measured at 1.7 K after the baseline test (empty squares), after storing the cavity in air for four months and filling with H_2 at 1 atm for 11 h (red triangles), after baking twice in H_2 at 1 atm at 120°C for 12 h (blue squares), after heat treatment at 600°C for 10 h in UHV (green diamonds), and after baking at 120°C for 12 h in UHV (empty diamonds). The arrows indicate the quench fields in the various tests. There was no field emission in any of the tests.

In order to accentuate hydrogen diffusion through the oxide into Nb, we evacuated the cavity to $\sim 4 \times 10^{-7}$ mbar and backfilled it with scientific grade H_2 up to 1 atm. The cavity was baked in the hydrogen atmosphere at 120°C for 12 h, followed by high-pressure rinsing (HPR) and assembly. The rf test at 1.7 K showed an increase of the residual resistance by about a factor of 2 while the quench field was reduced to about 162 mT. We repeated the same baking procedure in 1 atm of H_2 and the subsequent rf test results at 1.7 K (shown in Fig. 8) did not show any significant change from the previous test after the first baking.

The next treatment consisted in degassing in the furnace at 600°C for 10 h, which is done at JLab to reduce the bulk hydrogen content. Hydrogen was the gas with the highest partial pressure in the furnace, at approximately 2.5×10^{-6} mbar after the temperature ramp-up to 600°C and at approximately 8×10^{-8} mbar before cooldown. The partial pressures of the main residual gases in the furnace and the temperature profile during the heat treatment are shown in Fig. 10. After the heat treatment, the cavity was degreased in a tank with ultrasonic agitation and high-pressure rinsed. No chemical etching, typically done after heat treatments, was done on the cavity surface. The results of the rf test at 1.7 K, shown in Fig. 8, are characterized by an increase of the residual resistance by ~6.5 nΩ and, most noticeably, by the reoccurrence of the high-field *Q* drop. Temperature maps show strong hot spots in the equatorial region of the cavity [Fig. 9(c)], in the same areas where they occurred before the baking for the baseline test. After the cavity was baked *in situ*, on the vertical test stand, in UHV conditions at 120°C for 12 h, the *Q* drop was

---

[1] Details on the cavity preparation can be found in Ref. [15].

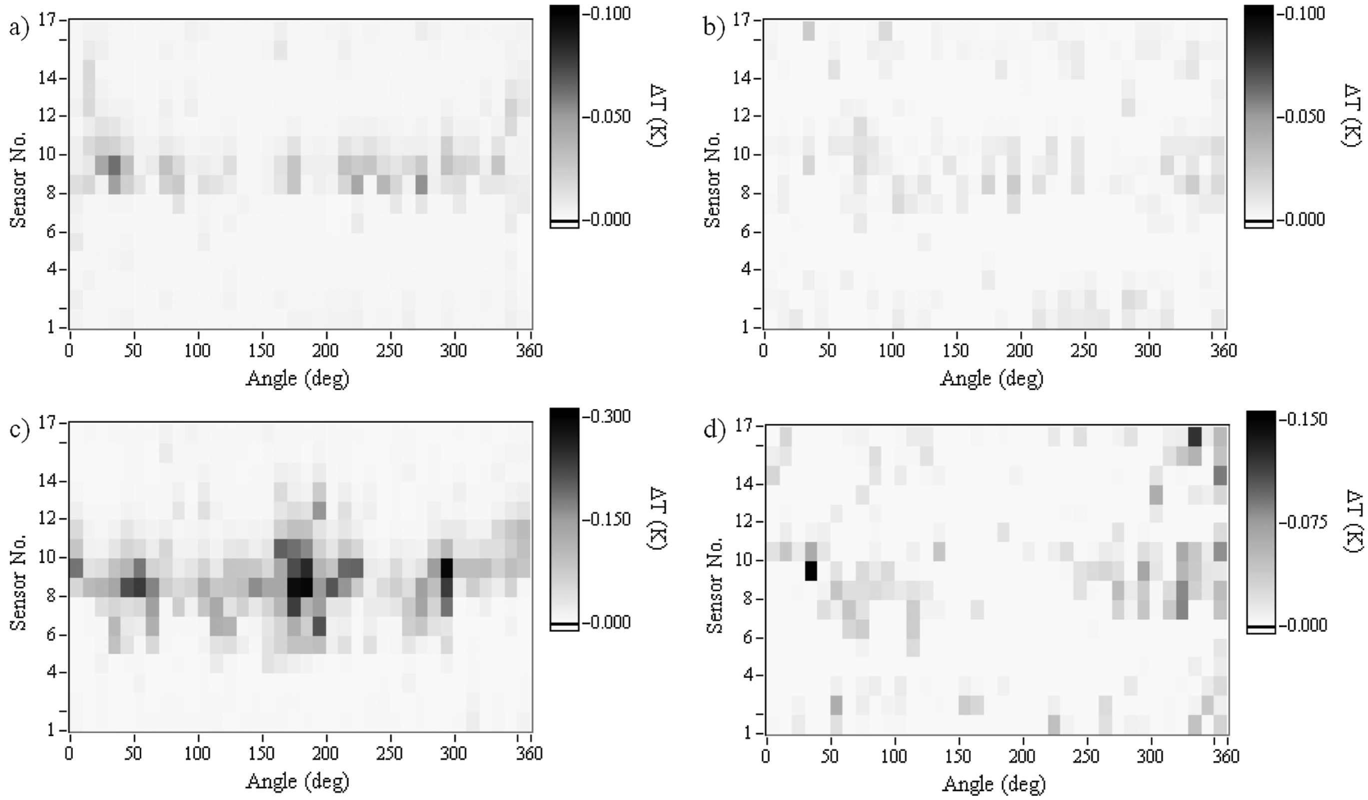

FIG. 9. “Unfolded” temperature maps at 1.7 K at the highest field achieved in the high-power rf tests of a large-grain CEBAF single-cell cavity (Q_0 vs B_p data shown in Fig. 8) after storing in air for four months and filling with H_2 at 1 atm for 11 h (a), after baking twice in H_2 at 1 atm at 120°C for 12 h (b), after heat treatment at 600°C for 10 h in UHV (c), and after baking at 120°C for 12 h in UHV (d). Note the different ΔT scales. Strong hot spots causing the Q drop are visible in (c). Sensors No. 1 and 16 are located at the top and bottom iris of the cavity, respectively, while the equator weld is between sensors No. 8 and No. 9.

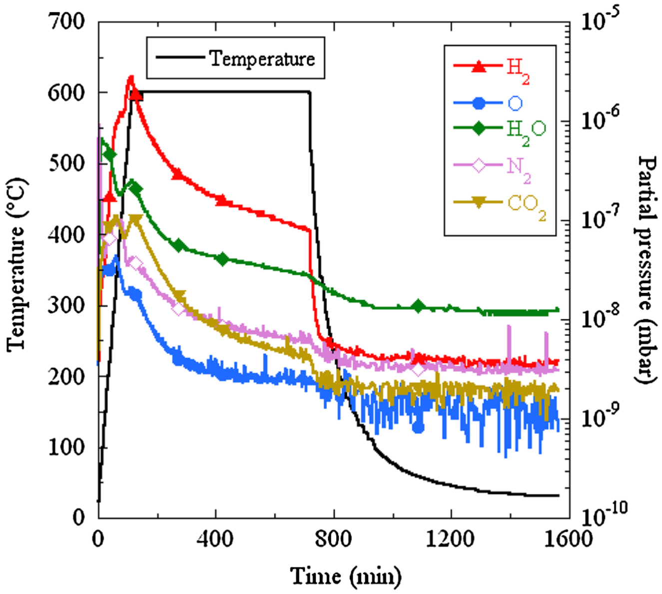

FIG. 10. (Color) Partial pressure of the residual gases and temperature profile during the 600°C/10 h heat treatment.

eliminated up to a quench field of 156 mT (data are shown in Fig. 8) and the temperature maps show much lower heating [Fig. 9(d)]. The quench location was, for all tests, in the region at the angles 20°–30°, sensors No. 8–9.

The values of the residual resistance R_{res} and energy gap Δ at 0 K divided by the product of the Boltzmann constant k_B and the critical temperature T_c obtained from a fit of $R_s(T, 10\ \mathrm{mT})$ between 4.3 and 1.7 K are shown in Table II. The data have been fitted with the usual sum of R_{res} and the BCS surface resistance, R_{BCS}. A T_c value of 9.25 K, a London penetration depth value at 0 K of 42 nm, and a coherence length value of 31 nm were fixed parameters in the fit. The occurrence of the Q drop correlates well with a reduction of the energy gap, as found in [15].

V. EXPERIMENTAL RESULTS ON NB HEAT TREATMENTS

A. Cavity test results

As it was discussed in Sec. II, it is clear that a significant improvement of the cavity performance, both in terms of quality factor and maximum accelerating gradient, should

TABLE II. Weighted average values of R_{res} and Δ/kT_c and l obtained from fits of $R_s(T)$ data after various treatments.

	R_{res} (nΩ)	Δ/kT_c	l (nm)
Baseline	10.2 ± 0.5	1.94 ± 0.01	17 ± 74
Storage in 1 atm H_2 for 11 h	6.0 ± 0.5	1.92 ± 0.04	16 ± 92
First baking at 120°C for 12 h in 1 atm H_2	12.0 ± 0.5	1.92 ± 0.06	17 ± 150
Second baking at 120°C for 12 h in 1 atm H_2	12.0 ± 0.5	1.894 ± 0.006	18 ± 88
Heat treatment at 600°C for 10 h in UHV	18.7 ± 0.7	1.81 ± 0.01	51 ± 10
Baking at 120°C for 12 h in UHV	23.2 ± 0.5	1.93 ± 0.01	18 ± 88

be achieved by reducing the amount of impurities and defects within a few hundred nanometers from the Nb surface. One way to accomplish this is to heat treat the cavity at high temperature (~ 800°C) for a few hours in a UHV furnace. Such heat treatment would reduce the density of lattice defects, such as dislocations and vacancies, reduce the amount of interstitial hydrogen, and dissociate the oxide layer, leaving only 1–2 monolayers of NbO on the surface.

One problem with this approach is that residual gases inside the furnace would be reabsorbed by Nb upon cooldown and subsequent exposure to air and water. A way to overcome this had been already proposed at SLAC in 1971 and consists of forming a thin (~ 10 nm thick) nitride layer on the surface at some intermediate temperature (~ 400°C) by thermal diffusion of nitrogen during the furnace cooldown [41]. The expectation is that the nitride layer would "passivate" the Nb surface and prevent hydrogen and oxygen absorption from the atmosphere. The nitride layer should be thin enough not to change significantly the superconducting properties of Nb. Of course, no chemical etching should be done afterwards. A calculation based on the solution and diffusion of nitrogen in niobium, detailed in Ref. [41], showed that it should be possible to grow a nitride layer about 10 nm thick on the Nb surface by admitting a N_2 partial pressure of about 5×10^{-6} Torr at 400°C for 15 min.

1. Large-grain CEBAF single-cell cavity

We attempted this process first on the large-grain single-cell cavity used for the experiments described in Sec. IV. The cavity was heat treated at 800°C/3 h, then cooled to 400°C at which point a nitrogen partial pressure of about 1×10^{-5} mbar was maintained in the furnace for about 15 min. Then the furnace was cooled to room temperature. Hydrogen was the gas with the highest partial pressure in the furnace, at approximately 4.1×10^{-6} mbar after the temperature ramp-up to 800°C and at approximately 2.6×10^{-7} mbar before cooldown. Semiconductor grade nitrogen from a gas bottle was introduced into the furnace through a regulator and a needle valve. The output of the needle valve was connected to a port on the side of the furnace through a vacuum line. The partial pressures of the main residual gases in this line were 5×10^{-5} mbar of CO_2, 4.7×10^{-5} mbar of N_2, and 4.6×10^{-5} mbar of H_2O. A picture of the furnace with the nitridization cart connected to it is shown in Fig. 11. The main residual gases in the furnace and the temperature profile during the heat treatment are shown in Fig. 12. After the heat treatment, the cavity was degreased for 1 h, followed by HPR for 1 h. The high-power rf test results at 1.7 K are shown in Fig. 13, along with the performance in the baseline test, after 20 μm removal by BCP 1:1:2, prior to the heat treatment. The Q_0 at low field improved by about 50%, while the Q drop, although still present, started at a field about 16% higher than in the baseline test. No field emission was present in both tests. The low field Q_0 and the resonant frequency were measured while slowly warming the cavity between 6 and 20 K, and the surface resistance R_s and change in penetration depth $\Delta\lambda$ were calculated from the data. A fit of $\Delta\lambda(T)$ with the two-fluid model resulted in a value of $T_c = 9.52 \pm 0.15$ K and of $\lambda(0)$ (the penetration depth at 0 K) equal to 64 ± 1 nm. The average value of R_s

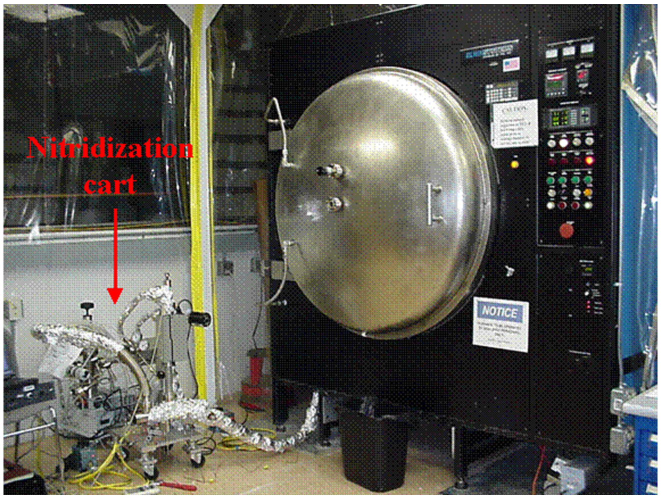

FIG. 11. (Color) Nitridization cart holding a semiconductor grade nitrogen gas bottle, pressure regulator, and needle valve connected to the high-temperature vacuum furnace used for the cavity heat treatments.

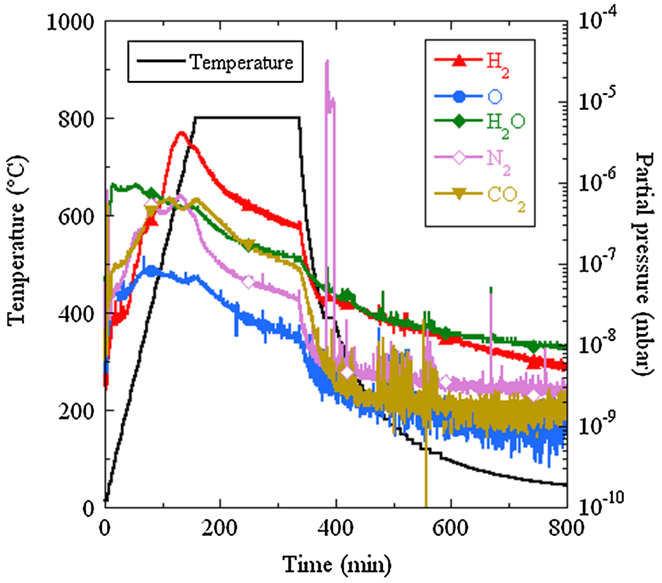

FIG. 12. (Color) Partial pressure of the residual gases and temperature profile during the cavity heat treatment. Nitrogen was injected into the furnace at 400°C for 15 min.

between 9.5 and 10 K was about 9 ± 7 mΩ, corresponding to a surface RRR of only 10 + 135 − 7. There was no other transition between 9.5 and 20 K.[2] The cavity was then baked *in situ* at 120°C for 12 h and tested again at 1.7 K. The results, shown in Fig. 12, indicate an improvement of the Q_0 at high field. A small amount of field emission (radiation level <4 mR/h) was detected above $B_p =$ 115 mT ($E_p = 46$ MV/m). Temperature maps were measured during each of the three rf tests and showed a major hot spot over the area between angles 150°–180° and sensors 6–9 [similar to a hot spot shown in Fig. 9(c)] during the baseline test. The area and intensity of this hot spot was reduced by the high-temperature heat treatment, while more uniform heating over the cavity surface was observed after the additional *in situ* baking.

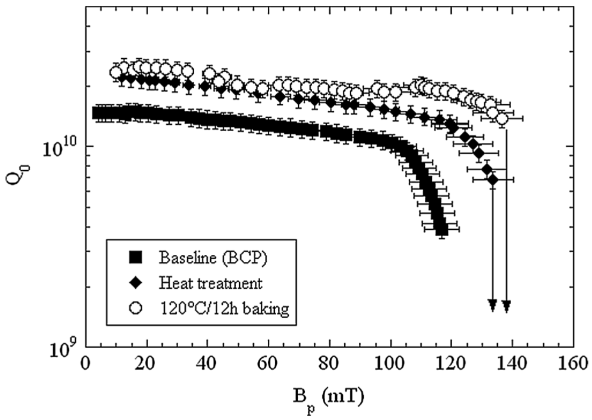

FIG. 13. Q_0 vs B_p measured at 1.7 K on a large-grain CEBAF single-cell cavity after the baseline test (squares) and after the 800°C/3 h, 400°C/20 min with 1×10^{-5} mbar N_2 injection heat treatment (triangles). The round symbols are the data after additional *in situ* baking at 120°C for 12 h.

A new baseline was established by removing about 5 μm from the inner surface of the cavity by BCP 1:1:2 and about 2 μm from the outer surface by BCP 1:1:1. The rf test results at 2 K are shown in Fig. 14 (the plot is labeled "Baseline 2"). The cavity was limited by Q drop, without field emission, starting at $B_p = 98$ mT. The cavity was then heat treated with the same temperature profile as in the first test except that the cavity was held at 120°C for 6 h after the nitrogen injection at 400°C and before the final cooldown of the furnace to room temperature. For this treatment, the nitrogen line connected to the furnace was baked at 120°C for 2 days prior to the cavity heat treatment. The partial pressures of the main residual gases in this line were significantly lower than in the first attempt: the pressure of H_2 was 2.2×10^{-8} mbar, the pressure of H_2O was 2×10^{-8} mbar, the pressure of N_2 was 6.7×10^{-9} mbar, and that of CO_2 was 4×10^{-9} mbar. After the heat treatment the cavity was degreased for 1 h, followed by HPR for 1 h. The rf test results at 2 K are shown in Fig. 14 (labeled "Heat treatment 2"): the low-field Q_0 improved by about 26% while no Q drop was found up to a quench field of 118 mT. Temperature maps measured during the baseline test showed some hot spots in the equator region similar to the ones observed in the previous tests. These hot spots were significantly reduced after the heat treatment and the quench location was at location 20°, sensor 11. Temperature maps at the highest field achieved during the baseline and after the heat-treatment tests are shown in Fig. 15.

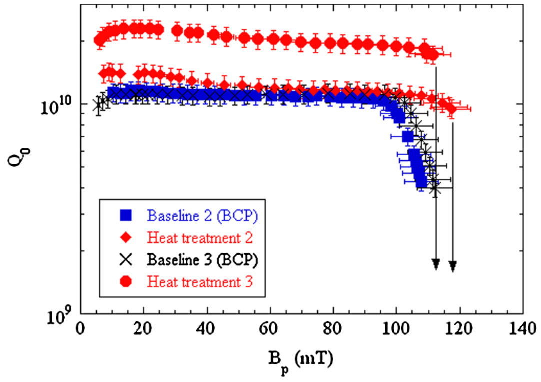

FIG. 14. (Color) Q_0 vs B_p measured at 2.0 K on a large-grain CEBAF single-cell cavity after two cycles of tests consisting of a baseline, established with BCP, and a heat treatment. "Heat treatment 2" consisted of the same process shown in Fig. 12 with the addition of holding the furnace at 120°C/6 h before final cooldown to room temperature. "Heat treatment 3" consisted of the same process shown in Fig. 12 but without N_2 injection.

---

[2] The critical temperature of NbN is about 16.5 K.

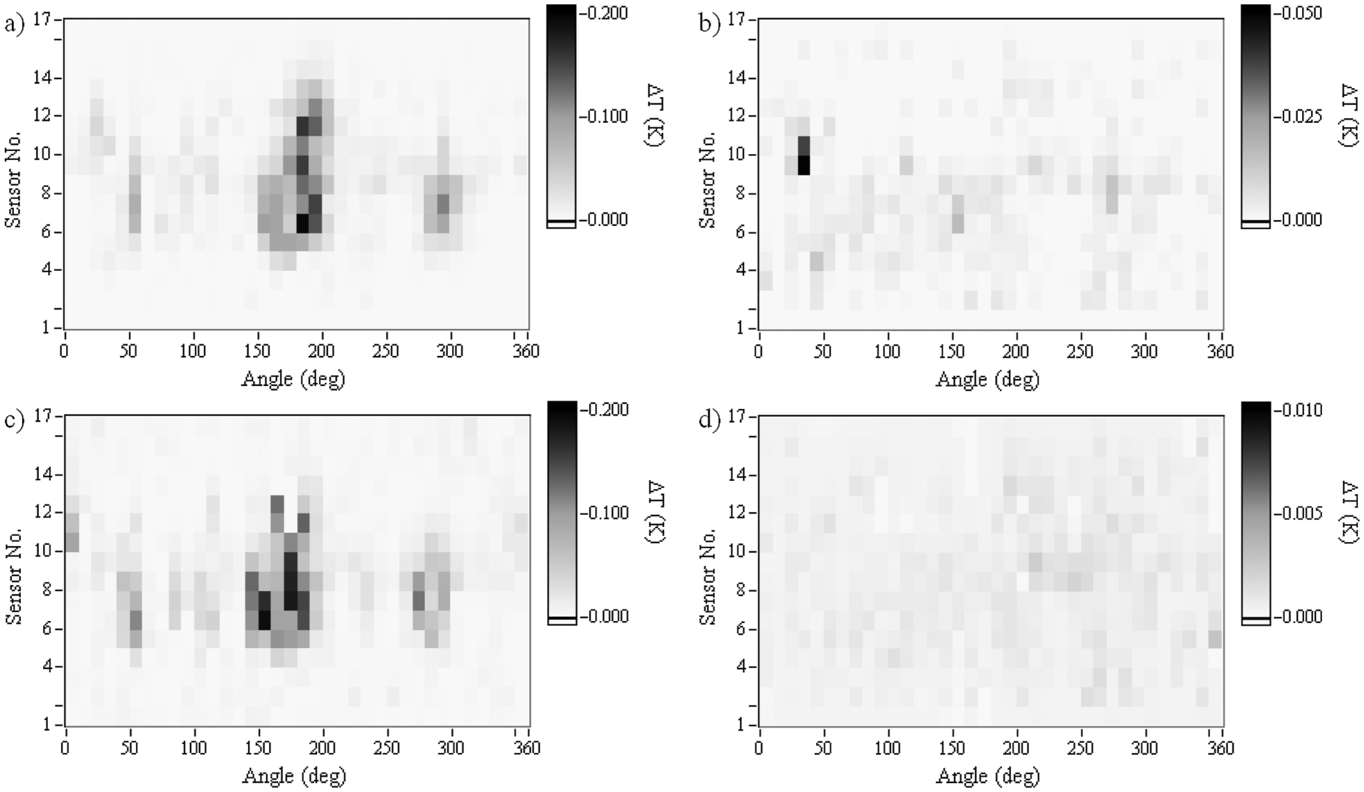

FIG. 15. Unfolded temperature maps at 2.0 K at the highest field achieved in the high-power rf tests of a large-grain CEBAF single-cell cavity after baseline tests 2 (a) and 3 (c) and after heat treatments 2 (b) and 3 (d). Note the different ΔT scales. Large hot spots present in the baseline tests are greatly reduced after heat treatments. Sensors No. 1 and 16 are located at the top and bottom iris of the cavity, respectively, while the equator weld is between sensors No. 8 and No. 9.

As will be discussed more in the next section, niobium samples which were heat treated with the cavity and analyzed by SIMS did not show the presence of any surface nitride layer after the first or the second heat treatment. Therefore we decided to repeat the heat treatment of the cavity with the same temperature profile as the first trial but without nitrogen injection. Prior to this a new baseline was established by removing about 2 μm from the inner and outer cavity surface by BCP 1:1:2. The rf test results, shown in Fig. 14 (labeled "Baseline 3"), were very similar to the previous baseline tests: Q drop occurred starting at $B_p = 100$ mT. The cavity was then heat treated at 800°C for 3 h, then cooled to 400°C and hold for 20 min before the final cooldown to room temperature. After the heat treatment the cavity was degreased for 1 h, followed by HPR for 1 h. Strong multipacting at $E_p = 36$ MV/m was observed during the subsequent rf test at 2 K and the cavity was subjected to another cycle of degreasing and HPR. The rf test results after this additional cleaning are shown in Fig. 15 (labeled "Heat treatment 3"): the low-field Q_0 improved by about a factor of 2 and no Q drop was measured up to a quench field of 112 mT. Temperature maps at the highest field achieved during the baseline and after heat-treatment tests are shown in Fig. 15 and show similar results as during the previous test. The quench location moved to location 240°, sensor 9. An optical inspection of this region did not reveal any outstanding geometrical feature.

2. Rolled single-crystal ILC single-cell cavity

The heat treatment with N_2 injection described in the previous section was applied to a 1.3 GHz single-cell cavity of the same shape as that of the center cell of the nine-cell cavity for the proposed International Linear Collider (ILC) project [42]. The single-crystal Nb disks from Heraeus, Germany, were prepared at DESY by few cycles of rolling and annealing to enlarge their diameter while maintaining a single-crystal structure [43]. The best rf performance of the cavity at 2 K can be found in [44] (named cavity #5) but it degraded after additional etching by BCP and was limited by Q drop to about 120 mT, after 120°C/12 h baking. Two noticeable features of this cavity were a rough, "orange peel" appearance of the inner surface after about 170 μm removal by BCP, and the persistence of the Q drop after baking at 120°C for 12 h. The cavity treatments prior to the baseline test consisted of 10 μm removal by BCP 1:1:2, heat treatment at 600°C for 10 h, followed by 13 μm removal by BCP 1:1:2. The rf test results at 2.0 K are shown in Fig. 16. The Q drop onset is at about 86 mT. The cavity was heat treated in the same

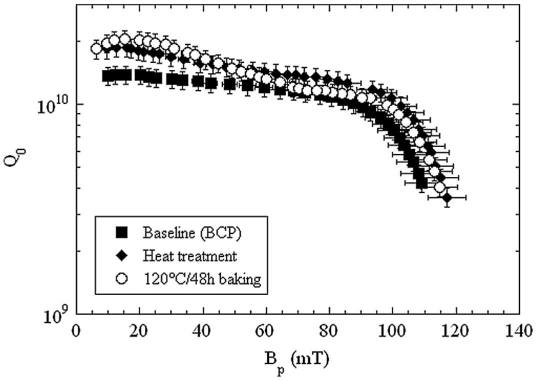

FIG. 16. Q_0 vs B_p measured at 2.0 K on a “rolled” single-crystal ILC single-cell cavity after the baseline test (squares) and after the heat treatment (triangles) at 800°C/3 h, 400°C/20 min with 1×10^{-5} mbar N_2 injection, 120°C/6 h. The round symbols are the data after additional *in situ* baking at 120°C for 48 h.

furnace run for the second heat treatment of the large-grain CEBAF cavity described in the previous section: the temperature was ramped to 800°C and held for 3 h, then dropped to 400°C as N_2 was injected for 15 min at that temperature, then the furnace was cooled to 120°C and held for 6 h before the final cooldown to room temperature. The cavity was then degreased for 1 h followed by HPR for 1 h. The rf test results at 2.0 K are shown in Fig. 16: the low-field Q_0 improved by about 35% but the *Q* drop was still present at about 10% higher onset field. The cavity was then baked *in situ* at 120°C for 48 h and retested at 2.0 K (the data are also shown in Fig. 16). The *Q* drop did not improve after the additional baking, consistent with earlier measurements reported in [44].

3. Fine-grain ILC single-cell cavity

The process of high-temperature heat treatment without subsequent chemical etching was tried also on a 1.3 GHz single-cell cavity built by Advanced Energy System (AES) from fine-grain Nb from Wah Chang, USA. The treatment before the baseline test consisted of vertical electropolishing [45] removing about 122 μm in three separate steps of the duration of 150 min each. The acid temperature was maintained at 25°C and the power supply voltage at 16 V, corresponding to about 30 A of current. The treatment was done by Curtis Crawford at JLab. The cavity then followed the standard cleaning procedure consisting of degreasing, HPR, drying, and assembly as the other single-cell cavities used for this study. The rf test results at 2.0 K are shown in Fig. 17: the *Q* drop onset was at about 107 mT. Brief multipacting occurred at $E_p = 37$ MV/m ($B_p = 86$ mT) but there was no field emission up to the highest measured field.

The cavity was then heat treated in the vacuum furnace at 800°C for 3 h, then cooled to 400°C and held for 20 min (no N_2 injection) at that temperature before the final cooldown to room temperature. Hydrogen was the residual gas with the highest partial pressure ($\sim 9.6 \times 10^{-6}$ mbar upon reaching 800°C and $\sim 2.4 \times 10^{-6}$ mbar before cooldown to 400°C) during the heat treatment. The cavity was then degreased for 1 h followed by 1 h of HPR. The rf test results at 2.0 K after the heat treatment are shown in Fig. 17: the low-field Q_0 improved by about 30% while the *Q* drop, although still present, shifted to about 8% higher field. No field emission was detected. The cavity was subsequently *in situ* baked at 120°C for 24 h and the following rf test at 2.0 K (also shown in Fig. 17) was characterized by a large reduction of the *Q* drop up to a quench field of 179 mT, close to the B_c value of Nb at 2.0 K.

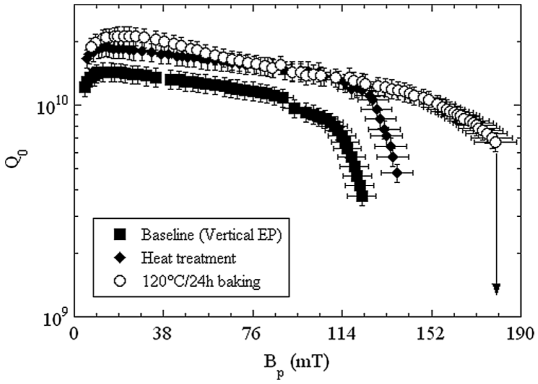

FIG. 17. Q_0 vs B_p measured at 2.0 K on the fine-grain ILC single-cell cavity “AES001” after the baseline test (squares) and after the heat treatment (triangles) at 800°C/3 h, 400°C/20 min. The round symbols are the data after additional *in situ* baking at 120°C for 24 h.

4. Large-grain ILC single-cell cavity

Another single cell used for this study was a 1.3 GHz cavity of the ILC shape built at JLab from large-grain Nb from Tokyo-Denkai, Japan. Earlier rf tests showed a quench field of about 136 mT, after the low-temperature baking at 120°C [46]. A new baseline was established by removing about 1 μm from the inner surface by BCP 1:1:2 and the rf test results at 2.0 K showed the *Q* drop starting at $B_p = 106$ mT (Fig. 18). The heat-treatment procedure was modified to eliminate the holding at 400°C for 20 min but to include the low-temperature baking by holding at 120°C for 12 h before the cooldown to room temperature. Hydrogen was the residual gas with the highest partial pressure ($\sim 1.2 \times 10^{-5}$ mbar upon reaching 800°C and $\sim 3.4 \times 10^{-7}$ mbar before cooldown to 120°C). After the heat treatment, the cavity was degreased for 1 h followed by 1 h of HPR. The rf test results at 2.0 K (Fig. 18) showed an improvement of the low-field Q_0 by about 74% while there was no *Q* drop up to a quench field of about 128 mT. Some multipacting activity was detected before and after the heat treatment at $E_p = 37$ MV/m ($B_p = 86$ mT), but there was no field emission in either test.

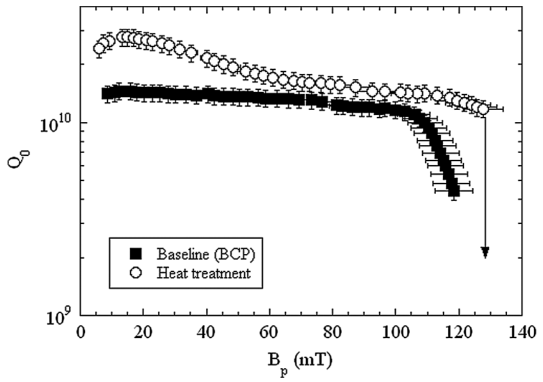

FIG. 18. Q_0 vs B_p measured at 2.0 K on a large-grain ILC single-cell cavity after the baseline test (squares) and after the heat treatment (circles) at 800°C/3 h, 120°C/12 h.

5. Summary of cavity rf test results

In Table III we summarize the rf test results by indicating the values of the Δ/k_BT_c, R_{res}, $R_{\text{BCS}}(4.3\text{ K}, \approx 10\text{ mT})$, $Q_0(100\text{ mT})$, the maximum value of B_p, and the improvement factor of both $Q_0(100\text{ mT})$ and $B_{p,\max}$ from the baseline test. The values of Δ/k_BT_c, R_{res}, and l were obtained from a fit of the $R_s(T, \approx 10\text{ mT})$ dependence, which was measured between 4.3 and 1.7 K during each cavity rf test. The typical error of the fit parameters Δ/k_BT_c and R_{res} were about 0.02 and 0.5 nΩ, respectively. The values of l were typically between 16–20 nm, with large errors (~ 100 nm). The typical error in the Q_0 and B_p measurements are about 10% and 5%, respectively. We report the improvement of the Q_0 values at $B_p = 100$ mT since that is the typical operating field chosen for SRF cavities in continuous wave energy recovery linacs.

The data reported in Table III indicate that the improvement of the Q_0 value at $B_p = 100$ mT is the result of a reduction of the BCS surface resistance while the R_{res} remained mostly unchanged by the heat treatment, without 120°C baking. The reduction of R_{BCS} is mainly described by an increase of the gap parameter in the data fit with the theoretical calculation of the BCS surface resistance. An increase of R_{res}, which is commonly observed after the low-temperature baking, compensates the further reduction of R_{BCS} after 120°C baking. The Q drop was still present after heat treatment, unless the 120°C baking was included, and the high-field performance of the cavities

TABLE III. Values of Δ/k_BT_c, R_{res}, $R_{\text{BCS}}(4.3\text{ K}, \approx 10\text{ mT})$, $Q_0(100\text{ mT})^{\text{a}}$, $B_{p,\max}$, and improvement factors of $Q_0(100\text{ mT})$, $B_{p,\max}$ over the baseline test for all the cavities and rf tests described in Secs. VA 1–VA 4.

Cavity	Treatment	Δ/k_BT_c	R_{res} (nΩ)	R_{BCS} (nΩ)	$Q_0(100\text{ mT})$ ($\times 10^{10}$)	$B_{p,\max}$ (mT)	Q_0 improvement	$B_{p,\max}$ improvement
LG CEBAF	Baseline 1 (20 μm BCP)	1.75	11.1	1068	1.05	118		
LG CEBAF	Heat treatment 1 (800°C/3 h, 400°C/20 min N_2)	1.87	10.3	825	1.52	134	45%	14%
LG CEBAF	Baking (120°C/12 h)	1.97	9.7	614	1.88	136	79%	15%
LG CEBAF	Baseline 2 (5 μm BCP)	1.79	5.6	971	0.91	108		
LG CEBAF	Heat treatment 2 (800°C/3 h, 400°C/20 min N_2, 120°C/6 h)	1.90	8.4	675	1.13	118	24%	9%
LG CEBAF	Baseline 3 (2 μm BCP)	1.80	7.9	933	1.07	112		
LG CEBAF	Heat treatment 3 (800°C/3 h, 400°C/20 min)	1.92	3.2	697	1.89	112	77%	0%
SC ILC	Baseline (10 μm BCP, 600°C/10 h, 13 μm BCP)	1.75	4.7	782	0.75	109		
SC ILC	Heat treatment (800°C/3 h, 400°C/20 min N_2, 120°C/6 h)	1.87	4.8	576	1.05	117	40%	7%
SC ILC	Baking (120°C/48 h)	1.98	8.2	414	0.94	115	25%	6%
FG ILC	Baseline (122 μm VEP)	1.80	5.7	724	0.92	122		
FG ILC	Heat treatment (800°C/3 h, 400°C/20 min)	1.85	4.5	656	1.46	137	59%	12%
FG ILC	Baking (120°C/24 h)	2.00	7.9	437	1.40	179	52%	47%
LG ILC	Baseline 3 (1 μm BCP)	1.83	4.9	831	1.16	119		
LG ILC	Heat treatment (800°C/3 h, 120°C/12 h)	2.00	4.2	412	1.44	128	24%	8%

[a] The values of $Q_0(100\text{ mT})$ were measured at 2.0 K, except for the first tests of the large-grain CEBAF cavity when they were measured at 1.7 K.

was limited by quenches at ~135 mT, most likely due to defects, and only on the fine-grain ILC cavity a significant improvement of $B_{p,\max}$ was obtained.

B. Niobium samples test results

1. Samples

Samples made of high-purity (RRR > 200) large-grain Nb from CBMM, Brazil (Ingot "D") and fine-grain Nb from Wah Chang, USA, with area $5\ \mathrm{mm} \times 7.5\ \mathrm{mm}$, 3.125 mm thick were cut by wire electrodischarge machining from larger disks. After cutting to dimensions, the samples were subjected to the following treatments: (i) etching by BCP 1:1:1, removing about 130 μm; (ii) etching by BCP 1:1:2, removing about 20–30 μm; (iii) heat treatment at 600°C for 10 h in the vacuum furnace; (iv) etching by BCP 1:1:2, removing about 10–15 μm; (v) nanopolishing at Wah Chang, USA.

The samples were heat treated with the cavities as indicated in Table IV. "Control" samples were not heat treated but were analyzed by SIMS in the same experimental conditions in which the heat treated samples were analyzed. The letter "F" in the sample code refers to fine-grain Nb, while the letter "L" refers to large-grain Nb.

2. SIMS analysis method

Secondary ion mass spectrometry (SIMS) is one of a limited number of surface analysis techniques that can detect hydrogen. Many of the analytical techniques used for elemental identification (energy dispersive spectroscopy, auger electron spectroscopy, x-ray photoelectron spectroscopy) cannot detect this element. Initial analyses on single-crystal niobium samples using ${O_2}^+$ and Cs^+ primary beams indicated apparent high levels of hydrogen and also showed the presence at high intensity of unusual species, ${NbH_x}^-$, where $x = 1$ to 5, for Cs^+ bombardment [47]. However, depth resolution and detailed interpretation were limited because of sample surface roughness.

A nanopolish procedure developed by Wah Chang (proprietary method) was able to provide niobium surfaces with mirror quality smoothness. With a large-grain sample prepared in this manner, it was possible to make a SIMS standard for C, O, and N in niobium. SIMS standards are typically made by ion implantation of the element of interest into a sample with matrix the same as the matrix to be analyzed [48]. In order to check the implant doses, a piece of (100) Si was implanted with C, N, and O at the same time. Because hydrogen was known to be at a high intensity in niobium from the earlier study, deuterium (D) was also implanted instead of hydrogen. The implanted samples showed typical Gaussian shaped curves for all four elements in silicon, but only for C, N, and O in niobium. The D profile in niobium showed no implant peak, indicating that the D is very mobile and can diffuse through the metal either without assistance or with the influence of the charged analysis beam [49]. Analysis of the SIMS standard provided relative sensitivity factors from which quantitative results for C, O, and N could be obtained. The niobium samples listed in Table IV were then analyzed under the same analysis conditions as the standard. Relative intensities for H and D were obtained and used to compare results for H.

Since Cs^+ provides enhanced secondary ion yields for H, C, N, and O, it is the beam of choice for analysis of these species and also avoids the problem of analyzing O with ${O_2}^+$ primary beam. ${O_2}^+$ and Cs^+ are the two beams generally available on SIMS depth profiling instruments because these two beams provide complementary analysis at ppma detection limits over the periodic table. All SIMS analyses were made using a CAMECA IMS-6F magnetic sector instrument and typical analysis current was 20 nA rastered over a $120\ \mu\mathrm{m} \times 120\ \mu\mathrm{m}$ region. Secondary ions were detected from a 30 μm diameter area at the center of the raster. Analyses were made with mass resolution 2000 ($m/\Delta m$ definition with 10% valley) to resolve the mass interference of H_2 with D, which requires a mass resolution of at least 1200. Negative secondary ions were detected in the form of depth profiles and mass spectra. It was necessary to monitor a molecular species, NbN^-, to detect N in niobium because the secondary ion yield for N^- is effectively zero. Depth determination of each crater was made using a Tencor P-10 stylus profilometer and these measurements were used to calibrate the depth axis. A uniform sputtering rate is assumed for the depth profiles.

TABLE IV. Heat treatment parameters of large-grain ("L" series) and fine-grain ("F" series) Nb samples with the single-cell cavities.

Cavity	Heat treatment	Heat treated samples	Control samples
LG CEBAF	800°C/3 h, 400°C/20 min N_2	L17, L18[a]	L19, L20[a]
LG CEBAF, SC ILC	800°C/3 h, 400°C/20 min N_2, 120°C/6 h	L13, L16	L14
LG CEBAF	800°C/3 h, 400°C/20 min	L10, L11	L9
FG ILC	800°C/3 h, 400°C/20 min	F1, F2, F3, F4	F5
LG ILC	800°C/3 h, 120°C/12 h	L6, L8	L14
none	600 °C/10 h	L5, L7	F5
none	600°C/10 h, 120°C/48 h	L7, F2	L14, F5

[a] These samples were not nanopolished.

Depth resolution for SIMS is typically improved by analysis at lower impact energy. Some of the initial analyses were made at Cs^+ impact energy of 6 keV and show improved depth resolution at the surface compared with 14.5 keV bombardment [49]. This condition was primarily used as a check for N at the surface after the initial nitrogen exposure experiments. However, most of the data reported here were obtained at Cs^+ impact energy of 14.5 keV as this operating condition provided improved count rates, which is important for species such as D^-, and the H^- and D^- profiles have typically shown constant levels which do not require improved depth resolution.

For each sample, a series of analyses were made. Because the SIMS analysis area is relatively small, at least two depth profiles were obtained from each sample. If there was a difference in intensity levels for these two profiles, then at least one more profile was obtained. For most samples, an additional profile using raster reduction was made. The raster reduction method consists of a depth profile where, after constant intensities have been achieved for the species of interest, the raster is reduced by approximately 50% in x and y, but the sputtering current is maintained. This increases the ion current density by approximately a factor of 4. If the intensity of a species increases by a similar factor after raster reduction, then one can conclude that that species is present in the sample at the concentration measured. If the intensity does not change, then the intensity observed is background. Changes between zero and approximately a factor of 4 increase indicate that the intensity is near background [48,50]. This raster reduction measurement is important because the species of interest in this study are residual gas species which are always present to some degree in the vacuum system. For some of the samples, especially the control samples, multiple sets of measurements were made. Mass spectra were also obtained on all the samples in order to check for $Nb_xH_y^-$ species and for contaminants.

3. *Results on samples*

Analysis was first made on samples L18 (after 800°C heat treatment and 400°C exposure to N_2) and L19 (control sample), and the implant standard. Samples L18 and L19 were not nanopolished and it was very difficult to make crater depth measurements. These analyses were made using low energy Cs^+ impact energy (6 keV) in order to check for the nitride layer. No nitride layer was detected. It was observed that the H^- count rate was approximately 2 orders of magnitude higher in the implant standard (which should be similar to a control sample) compared with sample L18. Sample L19 showed H intensity between L18 and the standard.

Because N was not detected in the first experiment, samples were analyzed from a similar experiment, but with an additional baking and with nanopolished samples. Sample L16 had 800°C/400°C N_2 exposure/120°C and L14 was a control sample. L14 was used as a reference sample for subsequent experiments. Once again the analysis was conducted at low Cs^+ impact energy and N was not detected. Both L14 and the control sample showed as much as 2 orders of magnitude more H than the heat treated sample. Results on these two samples were then repeated at higher Cs^+ impact energy (14.5 keV). Figures 19 and 20 show reduced data (concentration or counts versus depth) SIMS depth profiles for nanopolished samples L16 and L14, respectively. The H and D are very uniform with depth once we sputter below the surface. Depth axes for all of the figures are set at a maximum of 1.0 μm so that results on samples can be compared and the region near the

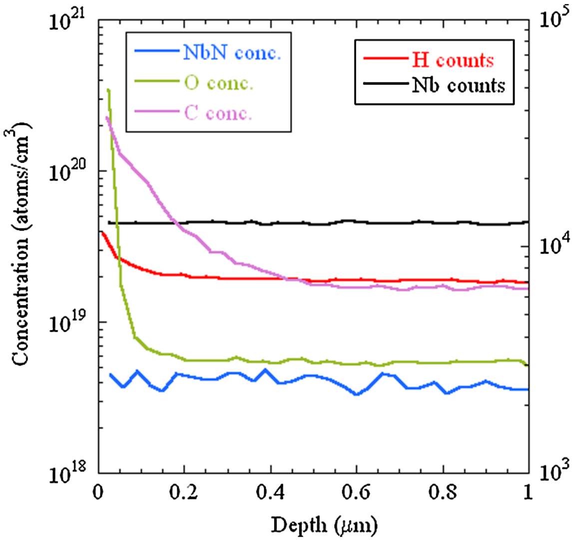

FIG. 19. (Color) SIMS reduced data depth profile for the heat treated sample L16. The heat-treatment parameters are 800°C/3 h, 400°C/20 min with N_2, 120°C/6 h (see Table IV).

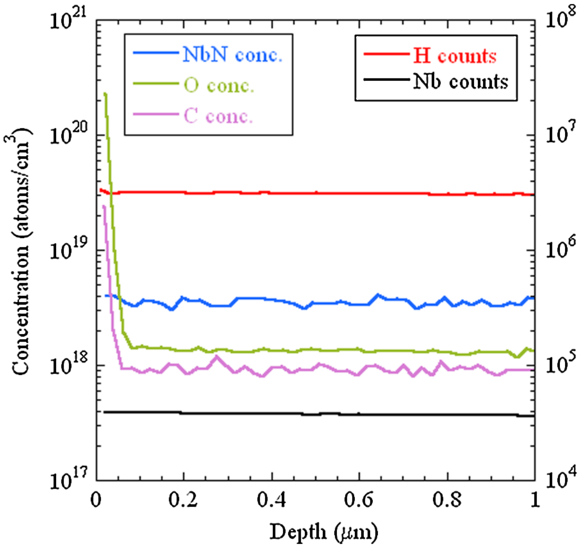

FIG. 20. (Color) SIMS reduced data depth profile for control sample L14.

TABLE V. SIMS H^-/Nb^- ratios for heat treated samples and corresponding control sample. All measurements at 14.5 keV Cs^+ except for first L16 measurement made at 6 keV Cs^+.

Cavity	Sample & heat treatment	H^-/Nb^- (sample)	Control	H^-/Nb^- (control)
LG CEBAF, SC ILC	L16: 800°C/h, 400°C/20 min N_2, 120°C/6 h	2.6	L14	102.2
LG CEBAF, SC ILC	L16: 800°C/h, 400°C/20 min N_2, 120°C/6 h	0.6	L14	82.9
LG CEBAF	L10: 800°C/3 h, 400°C/20 min	0.7	L14	89.7
FG ILC	F3: 800°C/3 h, 400°C/20 min	2.3	F5	75.6
FG ILC	F2: 800°C/3 h, 120°C/48 h	2.9	F5	81.0
LG ILC	L8: 800°C/3 h, 120°C/12 h	0.8	L14	80.6
None	L5: 600°C/10 h	2.9		
None	L7: 600°C/10 h, 120°C/48 h	1.4	L14	80.6
None	EP1 (small grain)	4.0	F5	81.0

TABLE VI. SIMS Measurements of C, N, and O, all at Cs^+ 14.5 keV.

Cavity	Sample & heat treatment	C (10^{18} at/cm^3)	N (10^{18} at/cm^3)	O (10^{18} at/cm^3)
LG CEBAF, SC ILC	L16: 800°C/h, 400°C/20 min N_2, 120°C/6 h	16	4.0	5.0
LG CEBAF	L10: 800°C/3 h, 400°C/20 min	13	3.4	5.3
FG ILC	F3: 800°C/3 h, 400°C/20 min	3.5	1.5	3.5
FG ILC	F2: 800°C/3 h, 120°C/48 h	2.8	2.6	4.2
LG ILC	L8: 800°C/3 h, 120°C/12 h	20	2.9	5.6
None	L5: 600°C/10 h	9.5	3.0	8.5
None	L7: 600°C/10 h, 120°C/48 h	7.4	3.0	7.8
None	EP1 small grain	2.9	2.4	2.8
	L14 control (average)	1.0	3.5	1.5
	F5 control (average)	0.35	1.6	1.5

surface can be viewed more clearly. Most of the profiles are at least several micrometers deep; profiles at least 6 μm deep were obtained. All of the species profiled showed no significant change with depth beyond the near surface region. D was monitored in this set of data and shows results that correspond with H. Examination of C, O, and N concentrations for the two samples shows there are differences in intensity, but not as large as the changes in H. C shows the largest change, about a factor of 10 more for the heat treated sample. It should be noted that the C, N, and O data are normalized to the Nb^- matrix ion signal and the Nb matrix signal is lower by about a factor of 3 for the heat treated samples compared with the control sample. The reason for the change in Nb^- intensity is not understood, but may affect the absolute accuracy of the C, N, and O concentrations for the heat treated samples because of the normalization to this species. No other more suitable alternative matrix ion has been identified. Raster reduction profiles showed that the H change matches that for the matrix Nb in L14 but is less for L16, indicating H in L16 approaches background. H/Nb count rate ratios and C, N, and O concentration for all analyzed samples are reported in Tables V and VI, respectively. C, N, and O concentrations are shown in the figures in terms of atoms/cm^3. Since the density of Nb is 5.5×10^{22} atoms/cm^3, the maximum concentrations below the surface of these three elements are all less than 5×10^{19} atoms/cm^3 or less than 0.1% atomic concentration.

Samples were then prepared without nitrogen exposure during heat treatment. Sample L10 was analyzed using

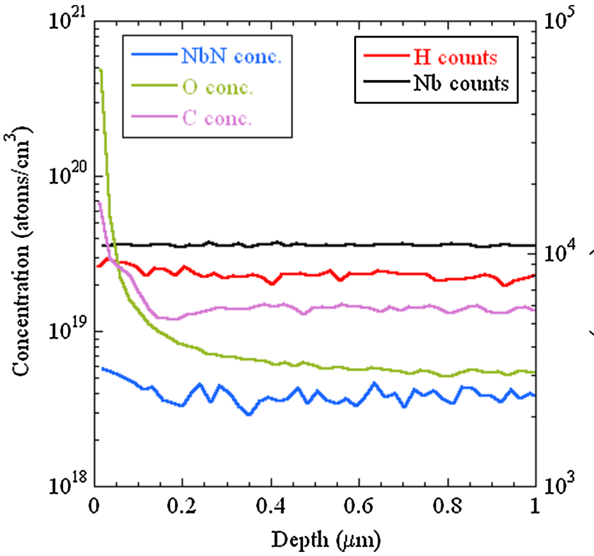

FIG. 21. (Color) SIMS reduced data depth profile for the heat treated sample L10. The heat-treatment parameters are 800°C/3 h, 400°C/20 min (see Table IV).

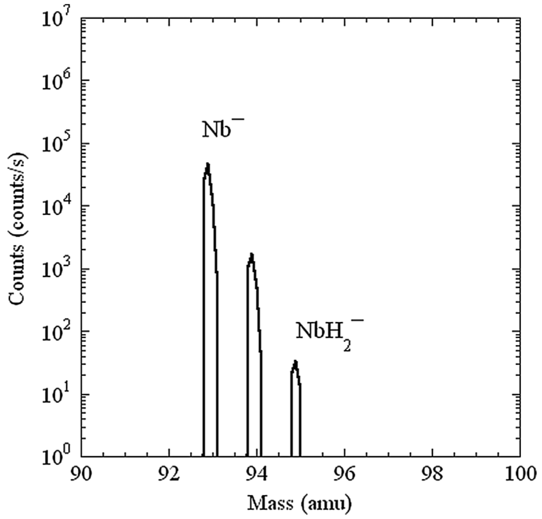

FIG. 22. SIMS mass spectrum of heat treated sample L10.

SIMS and the result is shown in Fig. 21. This profile is very similar to that for sample L16 which was exposed to N during 400°C heating and baked at 120°C.

Mass spectra were obtained on L10 and on the control sample L14. Figure 22 shows that the heat treated sample as received showed NbH_x^- species up to NbH_2^-. Other samples after heat treatment showed a similar spectrum. Figure 23 on the control sample shows high intensity species up to NbH_5^- were detected. The broad peak underlying the Nb peaks is thought to be a metastable species.

Sample L8 had been heat treated at 800°C and baked at 120°C during the same furnace run and the SIMS analysis (Fig. 24) showed similar H content to other large-grain samples heat treated at 800°C. NbH_5^- (mass 98) was also monitored in this profile and shows a constant value through the depth analyzed. Fine-grain samples F2 and F3 were heat treated with the same parameters as sample L10 and the reduced data SIMS depth profile of sample F3 is shown in Fig. 25: the hydrogen concentration is about a factor of 30 lower than the control sample (F5). Sample F2 was subsequently baked in UHV for an additional heat treatment at 120°C for 48 h and the SIMS analyses showed similar H content as sample F3. The H content of the fine-grain samples is higher than that of the large-grain sample for the same chemical and heat treatments.

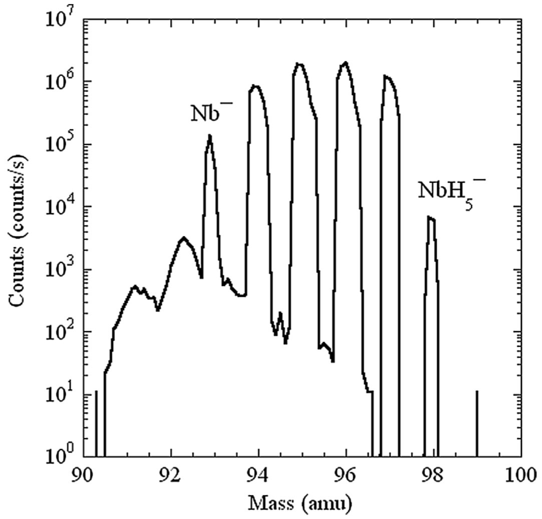

FIG. 23. SIMS mass spectrum of control sample L14.

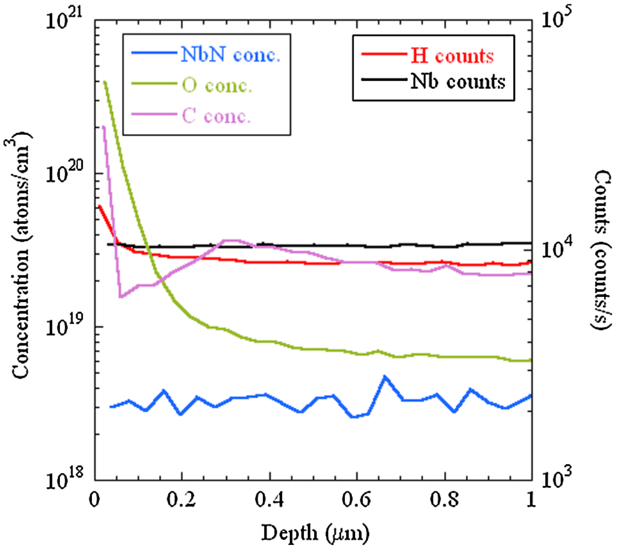

FIG. 24. (Color) SIMS reduced data depth profile for sample L8 (800°C/3 h, 120°C/12 h).

Samples which were heat treated to 600°C instead of 800°C were also analyzed. Figure 26 shows the reduced SIMS depth profile for sample L5, which indicates a similar but slightly higher H concentration than sample

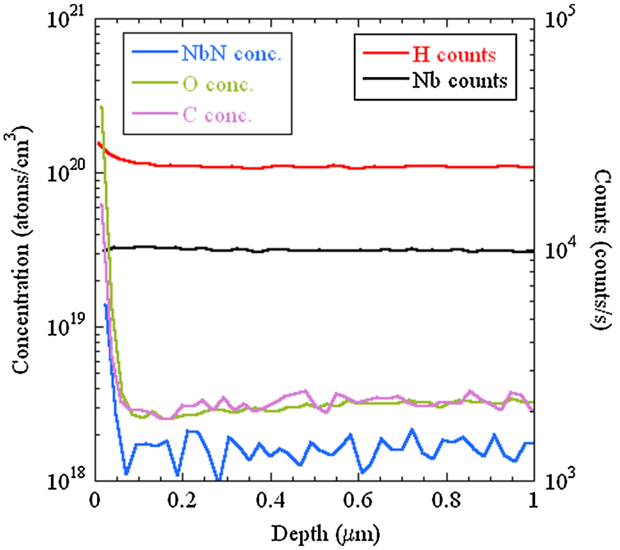

FIG. 25. (Color) SIMS reduced data depth profile for the fine-grain heat treated sample F3. The heat-treatment parameters are 800°C 3 h/400°C 20 min (see Table IV).

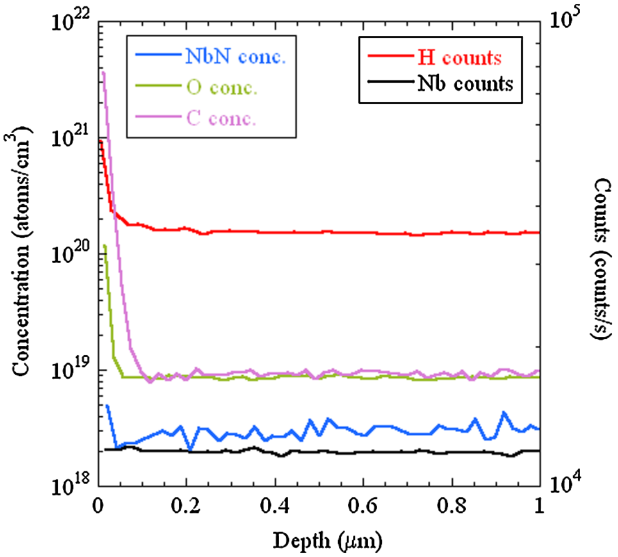

FIG. 26. (Color) SIMS reduced data depth profile for the heat treated sample L5. The heat-treatment parameters are listed in Table IV.

L10, which was heat treated at 800°C. Sample L7 (identical to L5) was then baked in UHV at 120°C for 48 h and the new SIMS analysis (Fig. 27) showed reduced H concentration by baking but still higher than sample L8, heat treated at 800°C and baked at 120°C for 12 h. Note that in this profile NbH_5^- was monitored and shows a constant intensity similar to the H^- profile.

The samples analyzed so far have been all processed with BCP etch before nanopolish. A sample was also analyzed after electropolishing but no additional heat treatment. Results for EP1 are shown in Fig. 28 and indicate the H level is significantly lower than for the control sample L14.

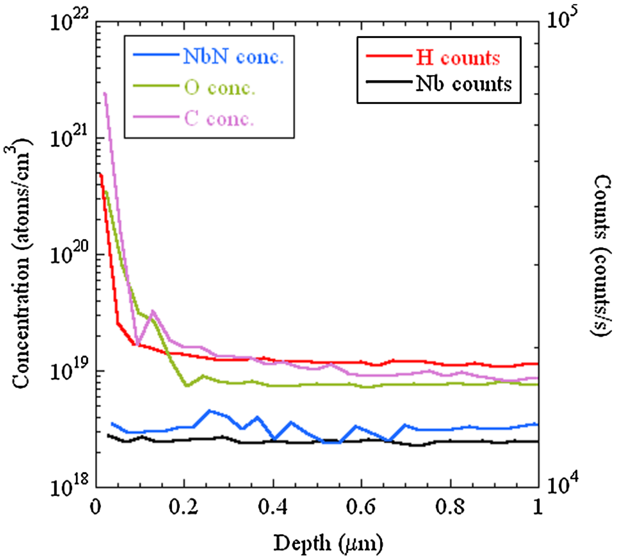

FIG. 27. (Color) SIMS reduced data depth profile for sample L7 (identical to L5) after additional 120°C/48 h baking.

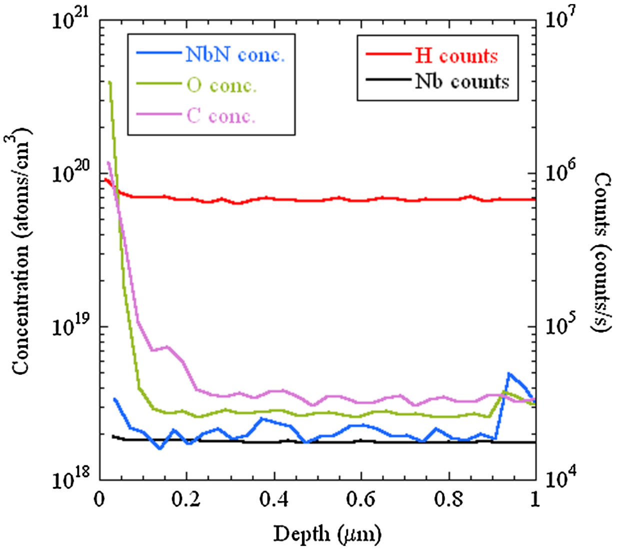

FIG. 28. (Color) SIMS reduced data depth profile for electropolished sample EP1.

VI. DISCUSSION OF EXPERIMENTAL RESULTS

Experimental results on the surface analytical investigation of the native oxide layer on low purity (RRR < 100) polycrystalline Nb had shown that the thickness of the oxide layer is nonuniform and oxidation along grain boundaries may proceed down to about 1 μm below the surface [51]. Cracks through the oxide may favor hydrogen absorption from the atmosphere and this explained results on Nb cavities of similar low purity for which the Q_0 degraded by long time exposure to air or exposure to hydrogen atmosphere for few hours [40]. This does not seem to be the case for high RRR Nb: images of the oxide layer by transmission electron microscopy (TEM) on both single-crystal [47] and fine-grain [15] Nb samples showed a very uniform oxide layer with thickness ranging from 5 to about 8 nm and no significant suboxide region. This was also confirmed by atom probe tomography (APT) [52]. The existence of a more uniform oxide layer on high-purity Nb provides a better protective layer against hydrogen absorption, as suggested by the results in Sec. IV on a cavity stored and baked in hydrogen atmosphere. Nevertheless, hydrogen absorption and/or desorption occurs during high-temperature heat treatments where the oxide thickness is reduced to a few monolayers. Although hydrogen desorbs from Nb at temperatures greater than about 550°C in UHV, it can be reabsorbed during the furnace cooldown to room temperature. For example, the hydrogen partial pressure before cooldown from Fig. 12 is about 2.67×10^{-7} mbar. This corresponds to a H concentration of about 3.7 at. % at room temperature, as calculated with Eq. (8). Of course this value is just an upper limit, as some of the hydrogen in the furnace chamber will be pumped out during cooldown. Hydrogen reabsorption and trapping at the metal/oxide interface may explain the occurrence of the *Q* drop in cavities that had been heat treated at 600°C (as shown in Sec. IV), 800°C (as shown in Sec. VA and in [53]), or 400°C (as shown in Ref. [16]) in UHV, without subsequent chemical etching.

While the standard processing of SRF cavities includes the removal of about 20 μm from the cavity surface after high-temperature heat treatment, because of potential Nb surface contamination from C, N, and O or residual metallic compounds from the furnace chamber, the results shown in Sec. VA indicate that improvements of the rf performance may be achieved by avoiding the chemical etching after the heat treatment. Of course, this may be possible only by using ''clean'' furnaces with good vacuum. The SIMS results indicate that the improvement of the cavity performance is correlated to a reduction of H concentration in Nb. The heat-treatment temperature should be high enough ($\geq 800°$C) to desorb tightly bonded H.

Surface-included hydrogen perturbs the electronic structure of the host metal, with the 1s electron that accompanies the hydrogen nucleus entering the s- and d-bands of the host metal, changing the density of states at the Fermi surface and causing shifts of the energy bands [54]. This may of course alter the superconducting properties of Nb and may be related to the anomalous zero-bias conductance observed in PCT experiments mentioned in Sec. II. The reduction of the BCS surface resistance after the high-temperature heat treatment may in fact be related to the reduction of this zero-bias conductance value, as observed for the 120°C baking. Since this phenomenon is not included in the theoretical calculations of the surface impedance based on the BCS theory, the reduction of R_{BCS} is fitted by an increased value of the gap parameter (see Table III).

The possibility of hydrogen generating vacancy clusters in Nb, due to lattice expansion, may also explain the presence of a higher defect density of chemically polished Nb surfaces shown by the EBSD data mentioned in Sec. II. While SIMS and NRA data indicate a reduction of hydrogen concentration after the 120°C baking, it is not clear in which direction it moves: it could either be detrapped from the surface, because of movement of interstitial oxygen and vacancies, and distribute uniformly within the bulk, or it may desorb from the surface through channels in the oxide during the partial decomposition of the Nb_2O_5 layer at the metal/oxide interface.

The SIMS analyses of fine-grain and large-grain samples treated by BCP and EP, before and after heat treatments, summarized in Tables V and VI, do not show significant differences in terms of C, N, and O concentration. There is an increase in C measured after heat treatment, but all of the concentrations of these elements measured below the oxide are less than 0.1% atomic. However, the SIMS measurements do show a trend with respect to H concentration, and this trend seems to correlate well with general cavity performance: (i) The H content is lower in BCP-treated large-grain Nb than in fine-grain Nb for the same heat-treatment parameters. (ii) Baking at 120°C further reduces the H concentration in Nb previously heat treated at 600°C. (iii) Fine-grain samples treated by EP have much lower H content than fine-grain samples treated by BCP.

Because of the sputtering technique used in SIMS measurements, H may readily diffuse through the crater from different directions, due to its high mobility, and is therefore difficult to observe the H peak at the metal/oxide interface, as detected with the NRA technique.

The passivation of the Nb surface by depositing a thin nitride layer by thermal diffusion of nitrogen introduced at low partial pressure at 400°C was not successful. Nitridation of niobium at 800°C with a nitrogen partial pressure of 10^{-2} mbar for 5 min or at 600°C for longer time, followed by rapid quenching of the furnace from the nitridation temperature to room temperature has been reported in the past [55]. The furnace available for the experiments described in this article is interlocked to prevent operation at high temperature if the pressure inside the chamber is greater than 10^{-4} mbar. Because a nitride layer of only few nanometers thick would be required for the passivation of the niobium surface, nitridation should be done at relatively low temperature to reduce nitrogen diffusion into the bulk. Therefore it may be necessary to increase the nitrogen partial pressure or to react Nb with dissociated nitrogen from a plasma. A more versatile furnace to try such experiments is planned to be installed at JLab.

VII. CONCLUSIONS

The understanding of the origin of anomalous rf losses (''*Q* drop'') in SRF Nb cavities operating at peak surface magnetic fields greater than about 90 mT has been an unsolved problem for about a decade. Analytical models which calculate the $R_s(B_p)$ dependence in the presence of ''defective'' regions of the Nb surface give a good description of the experimental data. Among the possible physical origins behind the *Q* drop mechanism, recent theoretical calculations and experimental results suggest the possibility of losses being generated by the motion of magnetic vortices, either pinned at the Nb surface or moving in and out of the surface in one rf period. Experiments to push pinned vortices deeper into the bulk by means of laser heating are being planned at JLab. From the material science point of view, which surface conditions may favor vortex pinning and/or penetration is not quite clear yet. Attempts to passivate the Nb surface by growing a thin nitride layer by thermal diffusion, as reported in this contribution, were not yet successful. Nevertheless, significant improvements of the rf cavity performance of several single-cell cavities was obtained after heat treatment at 800°C and 120°C, with no intermediate chemical etching. Nb samples treated with the cavities and analyzed by SIMS showed a very large reduction of H content after heat treatment. SIMS analysis also showed a good correlation between the rf performances of cavities with different crystallographic texture (large grain vs fine grain) and different chemical treatment (EP vs BCP) typically observed and the hydrogen concentration. More generally, there are experimental results on hydrogen reported in the literature which may be related to specific results on Nb samples which followed typical cavity preparation procedures. Of course, further high-quality research on this subject is necessary in order to fully understand the possible role of hydrogen in the Q drop and the baking effect.

ACKNOWLEDGMENTS

The authors would like to acknowledge A. Gurevich, FSU, and W. Weingarten, CERN, for many interesting discussions. From JLab, we would like to acknowledge P. Kneisel for providing the cavities for the heat-treatment study, C. Crawford for the vertical EP, D. Forehand and R. Overton for helping with the cavity heat treatments, and T. Harris and J. Davenport for helping with the cavity high-pressure rinses. This manuscript has been authored by Jefferson Science Associates, LLC under U.S. DOE Contract No. DE-AC05-06OR23177.

[1] P. Kneisel, K. Saito, and R. Parodi, in *Proceedings of the 8th Workshop on RF Superconductivity, Abano Terme, 1997*, edited by V. Palmieri and A. Lombardi (INFN, Legnaro, Italy, 2008) (LNL-INFN 133/98, 2008), p. 463.

[2] E. Kako, M. Bolore, Y. Boudigou, J.P. Charrier, B. Coadou, E. Jacques, M. Juillard, J.P. Poupeau, H. Safa, S. Noguchi, M. Ono, K. Saito, and T. Shishido, in Proceedings of the 8th Workshop on RF Superconductivity, Abano Terme, 1997 (Ref. [1]), p. 491.

[3] P. Kneisel, in *Proceedings of the 9th Workshop on RF Superconductivity, Santa Fe, NM, 1999*, edited by F. Krawczyk (LANL, Los Alamos, NM, 2000), p. 328.

[4] B. Visentin, J.P. Charrier, and B. Coadou, in *Proceedings of the 1998 European Particle Accelerator Conference, Stockholm, Sweden, 1998*, edited by S. Myers, L. Liljeby, Ch. Petit-Jean-Genaz, J. Poole, and K.-G. Rensfelt (Institute of Physics, Philadelphia, USA, 1998), p. 1885.

[5] G. Ciovati, in *Proceedings of the 13th Workshop on RF Superconductivity, Beijing, China, 2007*, edited by J.K. Hao, S.L. Huang, and K. Zhao (PKU, Beijing, China, 2008), p. 70.

[6] B. Visentin, in *Proceedings of the 11th Workshop on RF Superconductivity, Travemünde, 2003*, edited by D. Proch (DESY, Hamburg, Germany, 2004), TuO01; G. Ciovati, Physica C (Amsterdam) **441**, 44 (2006).

[7] M. Pekeler, in Proceedings of the 8th Workshop on RF Superconductivity, Abano Terme, 1997 (Ref. [1]), p. 822.

[8] A. Gurevich, Physica C (Amsterdam) **441**, 38 (2006).

[9] W. Weingarten, in Proceedings of the 13th Workshop on RF Superconductivity, Beijing, China, 2007 (Ref. [5]), p. 145.

[10] G. Ciovati, J. Appl. Phys. **96**, 1591 (2004).

[11] W. Weingarten (private communication).

[12] H. Safa, in *Proceedings of the 10th Workshop on RF Superconductivity, Beijing, Tsukuba, Japan, 2001*, edited by S. Noguchi (KEK, Tsukuba, Japan, 2002), p. 279.

[13] G. Ciovati, Appl. Phys. Lett. **89**, 022507 (2006).

[14] B. Visentin, in *Proceedings of the Pushing the Limits of RF Superconductivity Workshop, Argonne, 2004*, edited by K.-J. Kim and C. Eyberger (ANL, Argonne, IL, 2005) (ANL-05/10, 2005), p. 94.

[15] G. Ciovati, P. Kneisel, and A. Gurevich, Phys. Rev. ST Accel. Beams **10**, 062002 (2007).

[16] G. Eremeev and H. Padamsee, in Proceedings of the 13th Workshop on RF Superconductivity, Beijing, China, 2007 (Ref. [5]), p. 356.

[17] M. Delheusy, Ph.D. thesis, University of Paris-Sud IX and Stuttgart University, 2008.

[18] A. Gurevich and G. Ciovati, Phys. Rev. B **77**, 104501 (2008).

[19] G. Ciovati and A. Gurevich, Phys. Rev. ST Accel. Beams **11**, 122001 (2008).

[20] R.P. Huebener, Supercond. Sci. Technol. **8**, 189 (1995).

[21] A. Gurevich, at the 13th Workshop on RF Superconductivity, Beijing, China, 2007, http://accelconf.web.cern.ch/accelconf/srf2007/INDEX.HTML.

[22] A. Romanenko, G. Eremeev, D. Meidlinger, and H. Padamsee, in Proceedings of the 13th Workshop on RF Superconductivity, Beijing, China, 2007 (Ref. [5]), p. 173.

[23] B. Visentin, M.F. Barthe, V. Moineau, and P. Desgardin, in Proceedings of the 14th International Conference on RF Superconductivity, Berlin, Germany, 2009, paper TUPPO047, available from http://srf2009.bessy.de/html/author.htm.

[24] T. Proslier, J.F. Zasadzinski, L. Cooley, C. Antoine, J. Moore, J. Norem, M. Pellin, and K.E. Gray, Appl. Phys. Lett. **92**, 212505 (2008).

[25] S. Casalbuoni, E.A. Knabbe, J. Kötzler, L. Lilje, L. von Sawilski, P. Schmüser, and B. Steffen, Nucl. Instrum. Methods Phys. Res., Sect. A **538**, 45 (2005).

[26] R.E. Ricker, National Institute of Standards and Technology, Internal Report No. NISTIR 7635, 2009.

[27] C.Z. Antoine, S. Berry, and H. Shou, in Proceedings of the 11th Workshop on RF Superconductivity, Travemünde, Germany, 2003 (Ref. [6]), ThP05.

[28] B.J. Makenas, Metall. Trans. A **9**, 738 (1978).

[29] H. Behrens and G. Ebel, Gases and Carbon in Metals: Thermodynamics, Kinetics, and Properties. Pt. VIII, Group VA Metals (2), Niobium (Fachinformationszentrum Energie Physik Mathematik GmbH, Karlsruhe, Germany, 1976).

[30] K. Faber and H. Schultz, Scr. Metall. **6**, 1065 (1972); E.W. Hoyt, SLAC Technical Note No. SLAC-PUB-977, 1971.

[31] P. Chiggiato, G. Chuste, I. Wervers, and A.-M. Valente, JLab Technical Note No. TN-09-056, 2009.

[32] G.R. Myneni and S.R. Agnew, in *Proceedings of the 1st International Workshop on Hydrogen in Materials & Vacuum Systems, Newport News, Virginia, 2002*, edited

by G. R. Myneni and S. Chattopadhyay, AIP Conf. Proc. No. 671 (AIP, Melville, New York, 2002), p. 227.

[33] M. Hakovirta, CERN Technical Note No. CERN EST/2002-005 (SM), 2002.

[34] A. L. Cabrera, J. Espinosa-Gangas, J. Jonsson-Akerman, and I. K. Schuller, J. Mater. Res. **17**, 2698 (2002).

[35] R. J. Smith, Phys. Rev. B **21**, 3131 (1980); Y. Li, J. L. Erskine, and A. C. Diebold, Phys. Rev. B **34**, 5951 (1986); Bo-Shung Fang, C. A. Ballentine, and J. L. Erskine, Phys. Rev. B **36**, 7360 (1987).

[36] M. Lagos and I. K. Schuller, Surf. Sci. **138**, L161 (1984); M. Lagos, G. Martinez, and I. K. Schuller, Phys. Rev. B **29**, 5979 (1984).

[37] J. Čížek, I. Procházka, F. Bečvář, R. Kužel, M. Cieslar, G. Brauer, W. Anwand, R. Kirchheim, and A. Pundt, Phys. Rev. B **69**, 224106 (2004).

[38] U. Kobler and J.-M. Welter, J. Less-Common Met. **84**, 225 (1982).

[39] J. Knobloch, in *Proceedings of the 1st International Workshop on Hydrogen in Materials & Vacuum Systems, Newport News, Virginia, 2002*, edited by G. R. Myneni and S. Chattopadhyay AIP Conf. Proc. No. 671 (AIP, Melville, New York, 2002), p. 133.

[40] S. Isagawa, J. Appl. Phys. **51**, 6010 (1980).

[41] P. B. Wilson, SLAC Technical Note No. SLAC-TN-71-7, 1971.

[42] B. Aune *et al.*, Phys. Rev. ST Accel. Beams **3**, 092001 (2000).

[43] W. Singer, X. Singer, and P. Kneisel, in *Single Crystal-Large Grain Niobium Technology: Proceedings of the International Niobium Workshop, Araxá, Brasil, 2006*, edited by G. R. Myneni, T. Carneiro, and A. Hutton, AIP Conf. Proc. No. 927 (AIP, Melville, New York, 2006), p. 133.

[44] P. Kneisel, G. Ciovati, W. Singer, X. Singer, D. Reschke, and A. Brinkmann, in *Proceedings of the 2008 European Particle Accelerator Conference, Genoa, Italy, 2008*, edited by I. Andrian, O. Brüning, Ch. Petit-Jean-Genaz, and P. Pierini (EPS-AG, Mulhouse, France, 2008), p. 877.

[45] R. L. Geng, C. Crawford, H. Padamsee, and A. Seaman, in *Proceedings of the 12th Workshop on RF Superconductivity, Ithaca, USA, 2005*, edited by H. Padamsee (Cornell University, Ithaca, USA, 2007), ThP04.

[46] P. Kneisel (unpublished).

[47] A. D. Batchelor, D. N. Leonard, P. E. Russell, F. A. Stevie, D. P. Griffis, and G. R. Myneni, in Single Crystal-Large Grain Niobium Technology: Proceedings of the International Niobium Workshop, Araxá, Brasil, 2006 (Ref. [43]), p. 72.

[48] R. G. Wilson, F. A. Stevie, and C. W. Magee, *Secondary Ion Mass Spectrometry* (Wiley, New York, 1989).

[49] P. Maheshwari, H. Tian, C. Reece, G. Myneni, F. Stevie, M. Rigsbee, A. Batchelor, and D. Griffis, Surf. Interface Anal. (to be published).

[50] A. L. Pivovarov, F. A. Stevie, D. P. Griffis, and G. M. Guryanov, J. Vac. Sci. Technol. A **21**, 1649 (2003).

[51] J. Halbritter, Appl. Phys. A **43**, 1 (1987).

[52] K. E. Yoon, D. N. Seidman, P. Bauer, C. Boffo, and C. Antoine, IEEE Trans. Appl. Supercond. **17**, 1314 (2007).

[53] J. Knobloch, R. L. Geng, M. Liepe, and H. Padamsee, in Proceedings of the 9th Workshop on RF Superconductivity, Santa Fe, NM, 1999 (Ref. [3]), TUA004.

[54] A. C. Switendick, *Hydrogen in Metals I: Basic Properties*, edited by G. Alefeld and J. Volkl (Springer, Berlin, 1978), p. 101.

[55] M. Pham Tu, K. Mbaye, L. Wartski, and J. Halbritter, J. Appl. Phys. **63**, 4586 (1988).